Experimental Investigation of Controlled Rocking Cross-Laminated Timber Walls

By Matthew Robert Ficara, EIT, B.Eng

A Thesis Submitted to the School of Graduate Studies in Partial Fulfillment of the Requirements for the Degree Masters of Applied Sciences

Last Updated August 26, 2021

Abstract

Controlled rocking timber walls are being developed to resist earthquake loads without major structural damage. These systems respond to seismic loading through partial uplift from the foundation, dissipating energy through rocking impact and supplemental energy dissipation elements. Initial research and construction of these walls typically used Laminated Veneer Lumber (LVL); however, Cross-Laminated Timber (CLT) is increasing in popularity for controlled rocking timber walls, particularly in the North American market. Since the use of CLT in a rocking system is relatively new, it is important to understand how CLT behaves in this application. In particular, the area near the rocking toe is a critical region in a controlled rocking CLT wall, and the local deformations and strain distributions around the rocking toe are not yet well understood.

To address this issue, this thesis presents the results of an investigation of large-scale controlled rocking CLT walls subjected to quasi-static reverse-cyclic loading. The test specimens vary in terms of aspect ratio and applied axial load, so as to quantify how these differences affect the strain distribution in the rocking toe region at increasing levels of drift. The findings from this experimental procedure will aid in the understanding of current design models, as well as the development of better numerical models of the rocking toe, which are critical for the design and analysis of controlled rocking CLT walls.

Table of Contents

List of Figures

List of Tables

1 Introduction

1.1 Overview

Timber as a structural material has recently been regaining popularity due to engineering advancements, updates to building codes, and the ever-growing need to care for the environment through use of renewable resources. With regards to seismic applications, and the recent realization that design should focus on performance rather than only structural strength, recent research and advancements in lateral load resisting systems can be adapted for the utilization of timber.

Since sawn lumber has limitations for large scale construction, the use of engineered timber is required. Cross-laminated timber (CLT) is a relatively new engineered timber product that has become very popular across Europe, and is gaining popularity in the North American market.

One of the advancements in seismic research is the controlled rocking system. This controlled rocking concept introduces a moment resisting connection to the system, through the use of post-tensioned tendons, resulting in reduced seismic damage. These self-centering systems allow for isolated damage, ultimately resulting in a structure that is not only safe for its occupants post-seismic event, but is also economically efficient for building owners.

This study combines the concept of controlled rocking systems with CLT as a response to the current structural and seismic needs. Since the use of CLT in a rocking system is a relatively new concept, it is important to understand how CLT behaves in this particular application. Specifically, this study examines the behaviour of the area near the rocking toe, as it is a critical region in a controlled rocking system, and the local deformations and strain distributions around the rocking toe are not yet well understood.

Presented in this thesis are the results from tests of two large-scale CLT panels subjected to quasi-static reverse cyclic loading. Current numerical models, such as the Monolithic Beam analogy and the Winkler Spring analogy, were utilized to predict the behaviour of the rocking CLT wall. These models were than compared with the experimental results.

1.2 Scope of Research

The objective of this study is to develop an understanding of the performance and behaviour of cross-laminated timber used in a controlled rocking system, with a focus on the wall-foundation interface. In addition, current numerical prediction models and design procedures, commonly applied to concrete rocking systems, will be evaluated for their accuracy when applied to timber systems. In order to achieve this objective, the following must be completed:

- Design a prototype structure that will utilize a CLT controlled rocking system, following current Canadian design standards and other published guidance for seismic applications.

- Utilize the iterative moment-rotation analysis, updated for use with the Winkler Spring analogy to address the current short-comings of the Monolithic Beam analogy with regards to timber, to develop a prediction model. Emphasis will be put on the ease and time required to perform this analysis.

- Design, construct, and perform large-scale experimental tests and parametric studies on controlled rocking CLT panels to calibrate and evaluate the prediction model.

- Outline potential future research to further develop the knowledge of rocking CLT systems.

1.3 Thesis Organization

Chapter 2 provides an overview of the related topics, such as performance based earthquake design, cross-laminated timber, and controlled rocking system, while also reviewing related research and analysis methods.

Chapter 3 presents both the design of the prototype structure using the current Canadian design codes, as well as the design of the controlled rocking CLT panel using the iterative moment-rotation analysis and Winkler Spring analogy.

Chapter 4 outlines the experimental procedure and details pertaining to the test setup and data collection.

Chapter 5 reviews the data collected and discusses observations made during the testing procedure.

Chapter 6 compares and discusses the prediction model and experimental results.

Chapter 7 provides a summary of this experimental study and findings, and discusses potential

future research.

2 Literature Review

This section presents background information and previous studies related to the concept of controlled-rocking self-centering systems and the use of structural timber, specifically that of post-tensioned cross-laminated timber (CLT). This concept of a controlled-rocking system gained popularity in the 1990s with the Precast Seismic Structural Systems (PRESSS) program. Through the PRESSS initiative, various analysis methods and design approaches have been proposed for these systems. Past researchers have modified these analysis methods and design approaches in order to utilize these concepts for alternate structural materials.

2.1 Performance-Based Earthquake Engineering

Due to the recent realizations that increasing structural strength is not directly proportional to enhanced safety and reduced damage, the seismic design of structures has been reassessed, with more emphasis on performance as opposed to strength [Priestley, 2000]. This realization has paved the way to performance-based earthquake engineering (PBEE). The current concepts for PBEE, originally proposed by [SEAOC, 1995] and further developed by professional endeavors such as [ATC, 1996] and [FEMA, 2003]. PBEE relates the level of damage to a structure, up to and including collapse, along with any additional losses that result from from the structural damage, to the total cost to the owner. Through PBEE it can be expected that intelligent and informed decisions can be made, between both the client and engineer, based on life-cycle considerations rather than the construction costs alone [Krawinkler, 1999].

It is now clear that various performance objectives should be considered during seismic design. These performance objectives are organized into four categories: collapse prevention, life safety, immediate occupancy, and operational [NRCC, 2015]. Each category is associated with a specific damage state, where the required performance objective must be achievable by the structural design solution [Krawinkler and Miranda, 2004]. The parameters that define these damage states include floor displacements and accelerations, interstorey drift and structural member actions, and residual deformations [Reinoso and Miranda, 2005, Bradley et al., 2009, Pampanin et al., 2002]. In order to reduce the effect of these parameters, structural elements must be designed to remain elastic while

providing significant displacement capacity, while also minimizing and limiting residual displacements and floor accelerations [Newcombe, 2011]. The concept of PBEE can be visualized through an idealized pushover curve, presented by [Deierlein et al., 2003] in Figure 2.1.

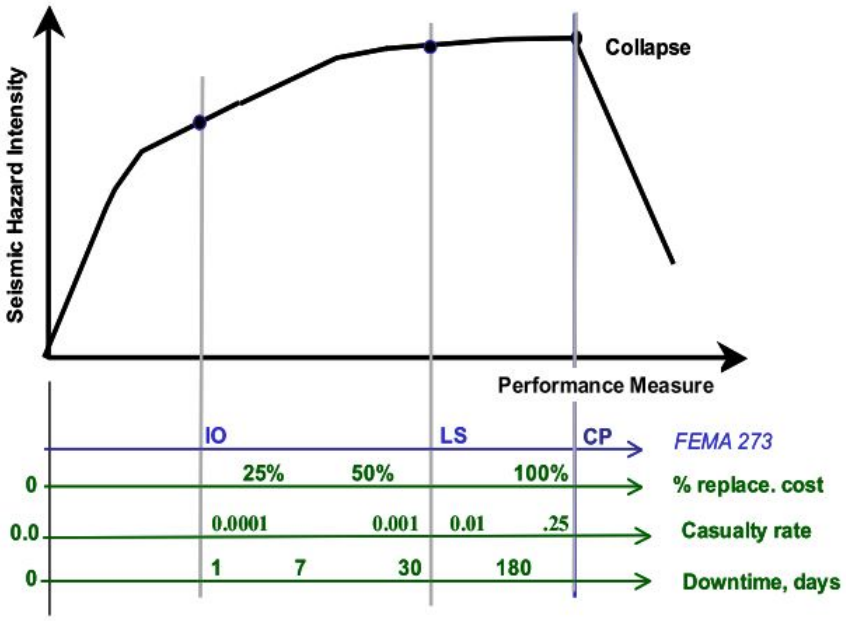

Figure 2.1: Idealized static pushover representation of seismic performance assessment [FEMA, 1997, Deierlein et al., 2003]

The pushover curve in Figure 2.1 is an early attempt by [FEMA, 1997] to relate the damage state parameters (displacements and accelerations, interstorey drift and structural member actions, and residual deformations) to the performance objectives: immediate occupancy (IO), life safety (LS) and collapse prevention (CP); though this relationship still remains an approximation [Deierlein et al., 2003].

The need for effective PBEE methodologies was evident from the aftermath of the 2010-2011 Canterbury, New Zealand earthquakes where the majority of buildings in the Christchuch Central Business District (CBD) had to be demolished and re-constructed [Bruneau and MacRae, 2017]. Occurring during peak occupational hours, the structures in the CBD and surrounding areas were subjected to severe seismic demands resulting in structural damage and the collapse of a six-storey office building [Bradley and Cubrinovski, 2011]. In addition to the devastating number of casualties,

it was reported that the rebuild costs were approximately $15 billion USD (10% of GDP), and insured losses were around US$25 billion USD [Parker and Steenkamp, 2012]. Although many structures that were damaged had been designed according to the current New Zealand standards, this event has made it apparent that the objective of preventing loss of life is no longer sufficient as a modern structural objective [Bruneau and MacRae, 2017].

As a relatively new lateral force resisting system, post-tensioned controlled rocking CLT walls should meet the objects of PBEE, minimizing losses while meeting the performance objectives decided upon by the owner and engineer.

2.2 Cross-Laminated Timber

Cross-laminated timber was first developed in the 1990s in Austria and Germany, and has become a very popular building material throughout Europe. By the early 2000s, the use of CLT increased initially due to the green building movement, as well as more efficient product manufacturing, product approval, and distribution. The benefits of of CLT can easily be noted through the various European structures built using CLT. Due to the prefabrication involved, and thus easy handling, quick construction time is achieved [Gagnon and Pirvu, 2011]. In recent years, CLT has become a more popular building material in Canada and continues to gain popularity as more research and building code updates are conducted.

Cross-laminated timber is an engineered wood product that consist of several layers, generally 3, 5, or 7, of sawn lumber glued together with alternating perpendicular layers that allows for high strength along both axes [Ganey, 2015], as shown in Figure 2.2. These products can easily be varied depending on the capabilities of the manufacturer. The sawn lumber is either visually or machine graded, and kiln dried. In order to maximize the wall resistance, the outer layers are oriented parallel to the direction of stress [Gagnon and Pirvu, 2011]. This manufacturing process is what separates CLT from other engineered wood products, which only have high strength in one direction [Gagnon and Pirvu, 2011, Ganey, 2015], and provides improved dimensional stability which allows for larger products to be manufactured [Gagnon and Pirvu, 2011]. The improved dimensional stability allows CLT to be used in larger projects where it might otherwise be assumed that timber would not be a viable material.

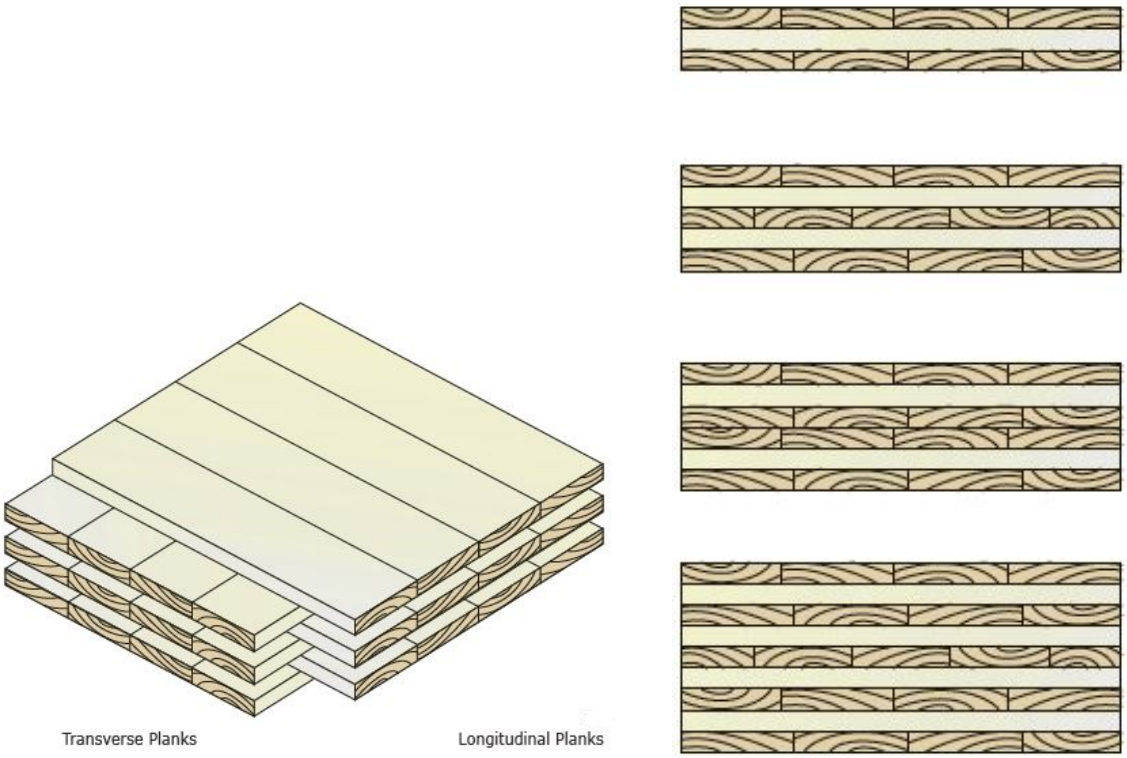

(a) CLT Panel Configuration [Gagnon and Pirvu, 2011]

(b) CLT Panel Cross-Section CLT Panel Configuration [Gagnon and Pirvu, 2011]

Figure 2.2: Cross-laminated timber design

Due to the large variation in available products, especially the vastly different species that grow in Canada as opposed to Europe, the mechanical properties of the individual boards, and thus the CLT panels, can vary. As a result of this variation, the majority of current design procedures are either analytical approaches that have yet to be fully verified, or those that are based on very specific experimental tests [Gagnon and Pirvu, 2011]. Some common approaches include the Gamma Method found in Eurocode 5 [European Committee for Standardization, 2004], the k-method by [Blass and Fellmoser, 2004], the Shear Analogy by [Kreuzinger, 1995], and CSA O86-14 approach [Canadian Standards Association, 2009]. In 2006, an Italian and Japanese joint initiative, referred to as the SOFIE project, conducted a study on the seismic behaviour of CLT construction. The project included cyclic, pseudo-dynamic and shake table tests on CLT wall panels and structures, shown in Figure 2.3. Around the same time, other forms of lateral load resisting systems using rocking

CLT were being developed, such as the PRES-LAM system that was an extension of the PRESSS program of the 1990's [Priestley, 1991, Priestley et al., 1999].

(a) Three-storey CLT house tested at NIED Laboratory, Japan [Gagnon and Pirvu, 2011]

(b) Seven-storey CLT building tested at E-Defense, Japan [Gagnon and Pirvu, 2011]

Figure 2.3: SOFIE project test structures

2.3 Controlled Rocking Systems

The concept of introducing a moment resisting connection through the use post-tensioned tendons in order to reduce seismic damage was originally developed during the Precast Seismic Structural Systems (PRESSS) program [Priestley, 1991, Priestley et al., 1999]. The PRESSS program examined both beam-to-column and wall-to-foundation connections. With the significance of residual deformations outlined in Section 2.1 in reference to the Christchurch Central Business District, the self-centering capabilities of this system are ideal for PBEE. For the wall-to-foundation systems, the post-tensioned cables connecting the wall to the foundation are activated by rocking during a seismic event. The post-tensioning force is transferred through the structure, helping it return to its original position after the seismic event [Newcombe, 2011, Kovacs and Wiebe, 2017].

During the PRESSS program, [Priestley et al., 1999] detailed various connections, with the hybrid connection showing the best performance: good ductility and minimal damage at large drifts [Ganey, 2015]. This connection included unbonded post-tensioning elements that allow for rocking and provide self-centering capabilities, and partially unbonded mild steel reinforcements to provide energy dissipation, shown in Figure 2.4a. The dual action between post-tensioning restoring capabilities and the energy dissipated by the mild steel results in the 'flag-shaped' hysteresis [Newcombe, 2011], Figure 2.4b.

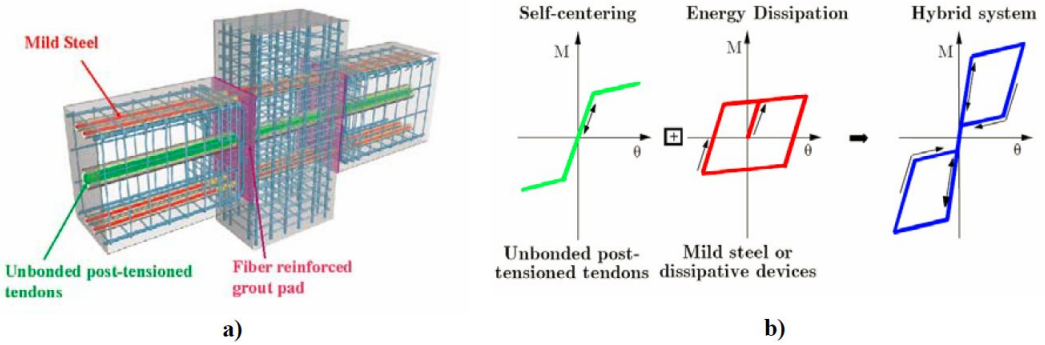

Figure 2.4: The PRESSS Hybrid Connection a) Beam-column connection (S. Nakaki) and b) Moment-rotation hysteretic response ([Fib, 2003]) - from [Newcombe, 2011]

[Sarti, 2015] outlines the general response of a rocking wall system, shown in Figure 2.5. As explained by [Sarti, 2015] and [Kovacs and Wiebe, 2017], the controlled rocking wall with only post-tensioning generally behaves in 4 stages. Stage 1, the wall is at rest with only gravity loads and the force from the post-tensioning, Figure 2.5a. During stage 2, after a force has been applied, the wall's deformation are those from bending and shear as the wall remains linear elastic, Figure 2.5b. Upon uplift, stage 3, the neutral axis depth begins to decrease. Stage 4 occurs when the neutral axis depth reaches the location of a tendon, and the post-tensioning force begins to increase, Figure 2.5d. This increasing force acts to return the wall to its original position through a moment that continues to increase as the post-tensioning force increases.

Although the main focus of the PRESSS program was on precast concrete [Priestley, 1991, Priestley et al., 1999, Kurama et al., 1999, Nakaki, S.D., Stanton, J.F., Sritharan, 1999, Kurama and Shen, 2004, Amaris Mesa, 2010], these concepts have also been adapted for steel [Christopoulos et al.,

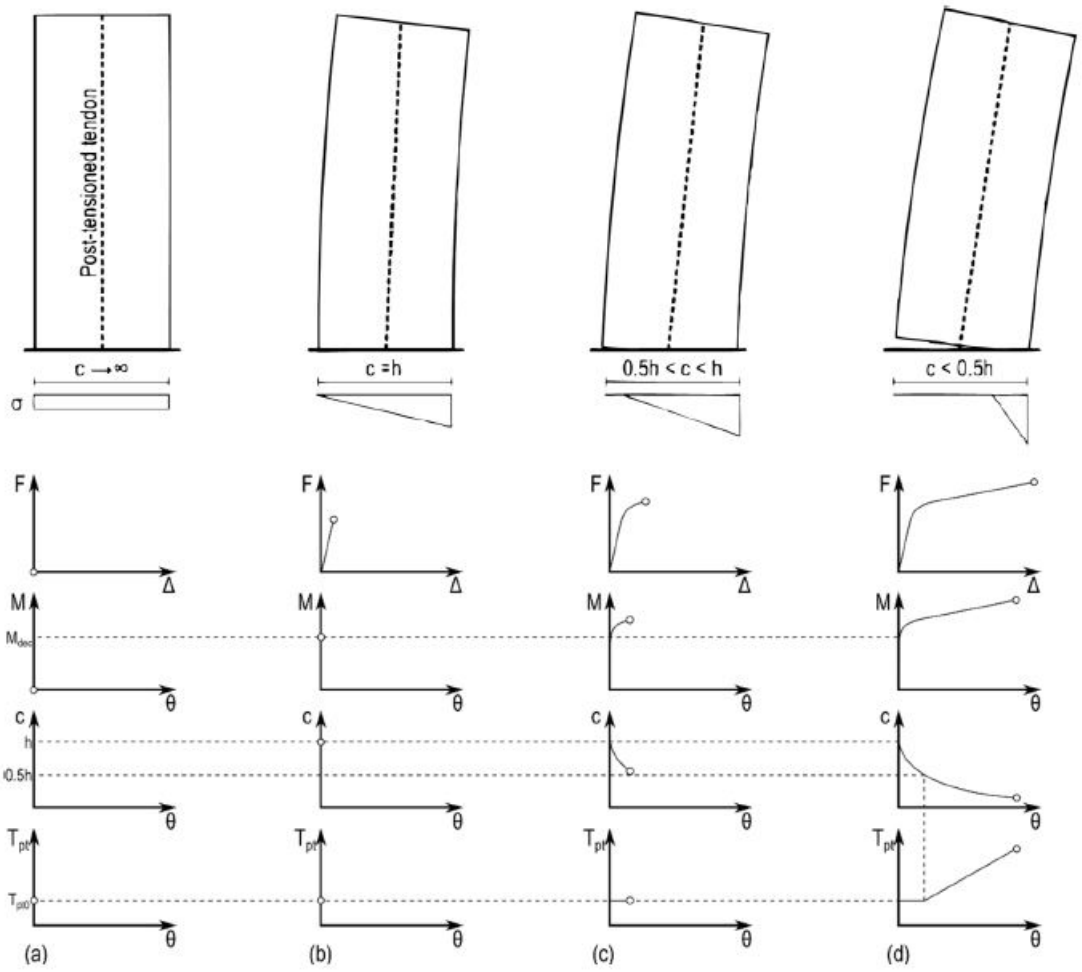

Figure 2.5: Controlled rocking wall response [Sarti, 2015]

2001, Ricles et al., 2001, Eatherton et al., 2008, Wiebe, 2013], and masonry [Laursen and Ingham, 2001, Laursen and Ingham, 2004, Rosenboom and Kowalsky, 2004]. The concept was later extended to timber elements in 2004 at the University of Canterbury by [Palermo et al., 2005] and further by [Newcombe, 2005, Palermo et al., 2006, Iqbal et al., 2007, Smith et al., 2008]. This extension of the hybrid connection to timber, specifically Laminated Veneer Lumber (LVL) and later glulam and CLT, was referred to as the Pres-Lam (pre-stressed laminated timber) system [Sarti, 2015]. Similar to [Kovacs and Wiebe, 2017], this research will focus on the rocking wall concept without supplemental energy dissipation, however, data gathered herein can be extended to alternative CLT

rocking wall design solutions, including those that use supplemental energy dissipation.

2.4 Previous Works on Controlled Rocking Timber Systems

The first tests on rocking timber wall systems were conducted by [Newcombe, 2005] and [Palermo et al., 2005, Palermo et al., 2006]. Both the post-tension only and the hybrid connection were tested under quasi-static cyclic and pseudo-dynamic loading procedures. The PT only walls were connected to the concrete base using two unbonded PT strands, while the hybrid connection also used both internal and external mild steel bars epoxied to the wall to dissipate energy. These walls were originally constructed using LVL. The wall-to-foundation subassembly, Figure 2.6a, displayed self-centering behaviour and energy dissipation, shown in Figure 2.6b, with little-to-no damage to the wall. In the tests conducted, the PT strands did not reach their yielding point, however, two of the three tests were stopped early due to buckling of the mild steel rods.

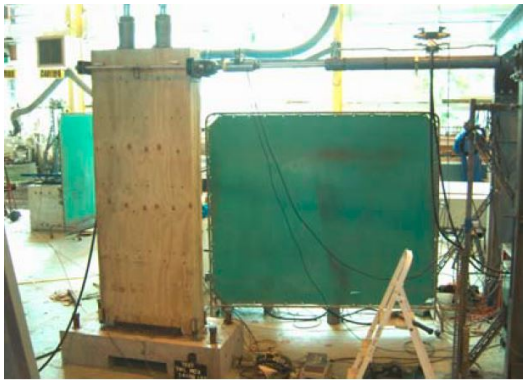

(a) Laboratory Test Setup [Palermo et al., 2006]

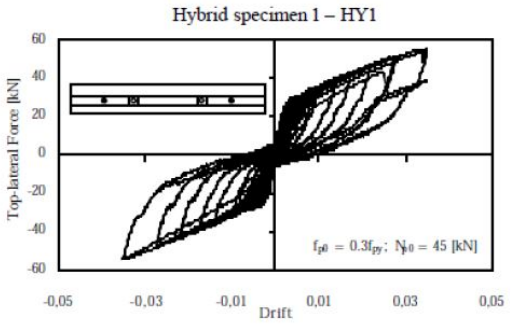

(b) Hybrid Specimen 1 - Lateral Force vs. Drift [Palermo et al., 2006]

Figure 2.6: Post-Tensioned Wall-to-Foundation Test from [Palermo et al., 2006]

These concepts were explored further when [Iqbal et al., 2007] replaced the mild steel dissipaters with U-shaped flexural plates (UFP), allwing for multiple walls to be coupled together, while still dissipating energy, as shown in Figure 2.7. UFP sizes were varied for multiple tests. With a test setup similar to [Palermo et al., 2006], the post-tensioned only and hybrid connections were tested using the UFP couplers. From these tests, [Iqbal et al., 2007] found that they were able to achieve a similar level of peak lateral force while using different values for energy dissipation. This was

achieved by altering both the arrangement of the UFPs and the level of stress in the PT strands. In addition, it was found that the hybrid connection achieved small peak displacements during the dynamic testing due to the energy dissipation from the UFPs. As expected from the rocking system, the system displayed self-centering behaviour with little damage. Similar to the tests performed by [Iqbal et al., 2007], [Smith et al., 2007] performed coupled wall tests using plywood sheets as the coupling device, shown in Figure 2.8.

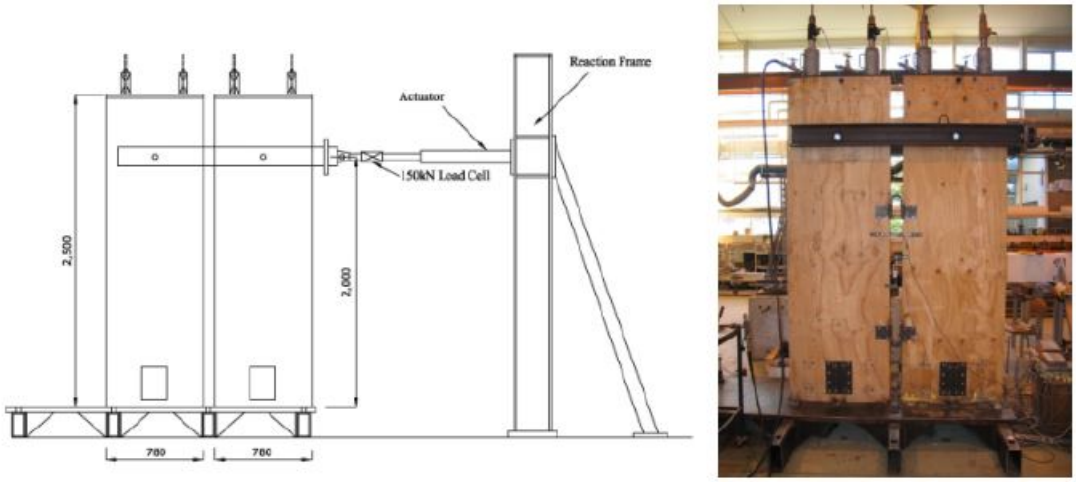

Figure 2.7: UFP Coupled Wall-to-Foundation Test from [Iqbal et al., 2007]

In 2008, [Smith et al., 2008] presented a theoretical re-design of the 6-storey concrete Biological Sciences building at the University of Canterbury, New Zealand, using LVL. The re-design incorporated the use of the beam-to-column and wall-to-foundation PRES-LAM systems originally proposed by [Palermo et al., 2005, Palermo et al., 2006]. The East-West direction would be composed of the hybrid beam-to-column connections limited to 2% drift, while the North-South direction would use the wall-to-foundation hybrid connection limited to 1% drift. The floor system was a timber composite deck design to transfer lateral loads to the LFRS. [Smith et al., 2008] performed a cost estimate that found that, although comparable, the cost of the structure using LVL was larger then that of steel and concrete. However, construction costs would be lower due to the prefabrication of the timber elements, which would result in quicker construction time with less workers on-site. In addition, these costs were based on the technology at the time. Engineered timber products, as well as their design methodologies, have developed greatly since the original estimate and thus, may result in a

Figure 2.8: Plywood Coupled Wall-to-Foundation Test from [Smith et al., 2007]

lower building cost.

[Marriott, 2009] continued the research of the post-tensioned wall-to-foundation setup by performing high-speed cyclic tests on single PT only and hybrid connection walls. Also included in these tests were fluid viscous dampers, in addition to the hysteretic mild steel dampers. The results from these tests showed a stable flag-shaped hysteresis, with the walls displaying full self-centering behaviour. [Marriott, 2009] proposed that the system incorporating both damping devices would prove beneficial in locations where there is a concern for near-field effects.

[Sarti, 2015] conducted research that focused on the prediction models for the peak forces and displacements of rocking LVL wall systems. The experimental stages incorporated component testing of both internal and external dissipaters, as well as varied post-tensioning arrangements. Tests were conducted on single wall-to-foundation arrangements, as well as a proposed alternative column-wall-column configuration designed to support the connecting floor diaphragm. [Sarti, 2015] used the data collected from these tests to refine and validate his analytical models for the use of the internal and external dissipaters in these systems, and evaluated the rotational and multi-spring numerical prediction models, discussed further in Section 2.5.

[Dunbar et al., 2013, Ganey, 2015] aided in expanding the concept of controlled rocking timber walls to CLT. [Ganey, 2015] performed a variety of single wall-to-foundation tests with variations in the PT area and initial force, CLT composition, and the rocking base. Additionally, a single test was performed on a UFP coupled wall. The tests followed a quasi-static reverse-cyclic loading protocol. The axial compression properties obtained via material tests are shown in Figure 2.9a, with the simplified response proposed by [Ganey, 2015] shown in Figure 2.9b.

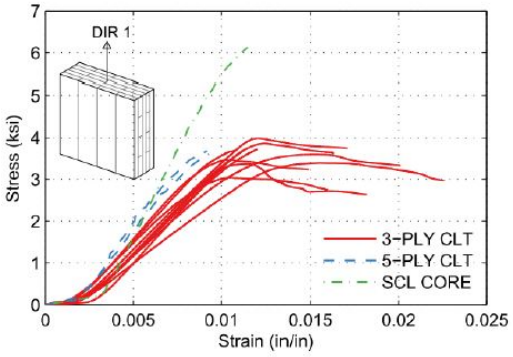

(a) Axial Compression Results for CLT [Ganey, 2015]

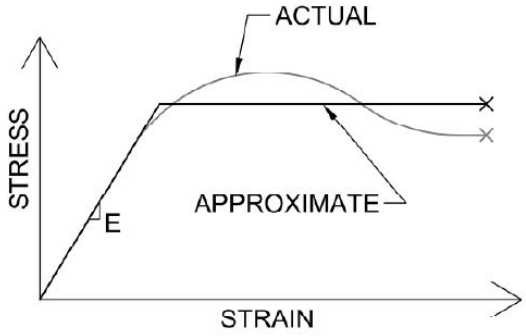

(b) Simplified Response Presented by [Ganey, 2015]

Figure 2.9: CLT Compression Results and Simplification [Ganey, 2015]

Following the experimental program, prototype structures were assessed using refined numerical modeling techniques in order to validate the design procedure using CLT. [Ganey, 2015] found that up to 5% drift, the self-centering capabilities and strength of the wall were unaffected. However, there was significant loss of PT force due to CLT damage and at large drifts (9%), significant damage in the toe region was observed. As a possible solution, [Sarti, 2015] recommends that steel bearing plates should be used in order to distribute the PT stress and potentially avoid issues with long-term creep and short-term local damage. From the numerical analysis, Ganey concluded that CLT rocking walls can provide sufficient self-centering behaviour and energy dissipation in regions of high seismicity for tall timber buildings.

In summary, the previous studies on controlled rocking timber systems have shown the desired self-centering performance with minimal damage. However, there is still a lack of data available to validate and calibrate numerical models for the rocking joint. There, this study aims to expand that experimental database, so as to better develop the analysis methods described in the following

section.

2.5 Analysis Methods and Design Approaches

A major issue with the refined modeling techniques presented by [Sarti, 2015, Ganey, 2015] is that they rely on experimental data for calibration [Kovacs and Wiebe, 2017]. As timber products are highly variable, experimental data would be required in every instance of a new design. As this is not a feasible approach to this issue, a general update to the modeling technique for the use of CLT could prove more useful.

2.5.1 The Monolithic Beam Analogy

The modeling technique used by [Sarti, 2015, Ganey, 2015] is known as the Monolithic Beam Analogy (MBA), originally proposed by [Pampanin et al., 2001], during the PRESSS program. The MBA was later modified by [Palermo and Pampanin, 2008] for use on post-tensioned precast concrete. The modified MBA was then adjusted by [Newcombe et al., 2008] for post-tensioned timber systems. The concept behind the MBA is that, due to the hybrid connection not satisfying the Bernoulli-Navier Hypothesis, a new concept was required to reduce the number of unknown variables [Newcombe, 2008]. The MBA achieves this through the analogy made between the hybrid connection and an equivalent strain compatible member (the monolithic beam), which focuses on the plastic rotation domain of the response [Newcombe, 2008]. The iterative moment-rotation analysis is outlined step-by-step in Figure 2.10.

Decompression Moment

When the connection moment is lower than the decompression moment, M_{dec}, there will be no uplift ($\theta_{gap} = 0$) and the wall will behave as a vertical cantilever. If the connection moment exceeds the decompression moment, the iterative moment-rotation analysis, shown in Figure 2.10, can be applied.

$$M_{dec} = (W + T_i)\ d \tag{1}$$

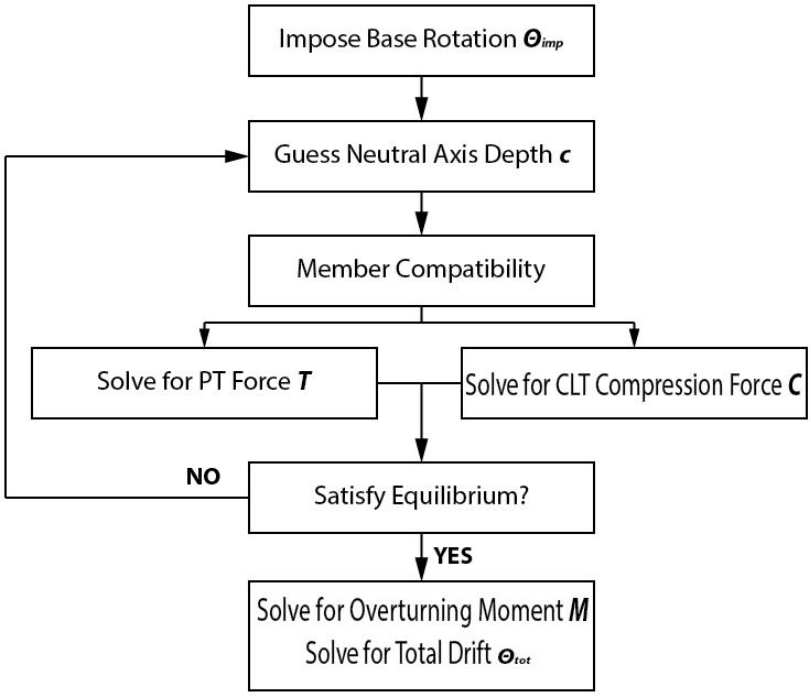

Figure 2.10: Iterative Moment-Rotation Analysis based on [Pampanin et al., 2001, Newcombe et al., 2008, Sarti, 2015, Ganey, 2015]

Where

W = Gravity Load

T_i = Initial Post-Tensioning Force located at the Center of Mass

d = Moment Arm

Before uplift, the elastic displacement can be calculated using the initial stiffness of the wall.

$$k_w = \left(\frac{h_w^3}{3E_w I_w} + \frac{h_w}{G_w A_w} \right)^{-1} \tag{2}$$

Where

h_w = Wall Height

E_w = Modulus of Elasticity

I_w = Second Moment of Area

G_w = Shear Modulus

A_w = Cross-Sectional Area

$$\Delta_e = \frac{M}{k_w h_w} \tag{3}$$

Where

h_w = Wall Height

k_w = Initial Stiffness

M = Connection Moment

The iterative moment-rotation procedure, Figure 2.10, can now be conducted.

1. Impose Connection Rotation, Θ_{imp}

An initial value for the connection rotation is chosen and applied to the structure. This chosen value signifies an instant in time when the wall has decompressed and gap between the base and wall has opened by the chosen value. By including the elastic displacement of the wall prior to decompression, the story drift can can be determined.

$$\Theta_s = \frac{\Delta_e}{h_w} + \Theta_{imp} \tag{4}$$

2. Assume Neutral Axis Depth, c

The neutral axis depth, c, is the length of wall that is in compression. Before the wall has decompressed, the neutral axis depth is equal to, or greater than the length of the wall. The estimated value will be iterated to achieve equilibrium.

3. Determine Post-Tensioning Force, T_{PT}

The PT force, T_{PT}, is the sum of the initial PT force, $T_{PT,initial}$, and the change in PT force, ΔPT.

$$T_{PT} = T_{PT,initial} + \Delta T_{PT} \tag{5}$$

The change in PT force is due to the elongation of the PT, Δ_{PT}, as the deflection and gap rotation increases.

$$\Delta_{PT} = \theta_{imp}(y_{PT} - c) \tag{6}$$

Where

y_{PT} = Distance from Wall Edge to PT

Therefore, to determine the change in PT force, the elongation of the post-tensioning element is multiplied by its axial stiffness , k_{PT}.

$$\Delta T_{PT} = k_{PT}\Delta_{PT} \tag{7}$$

4. Determine CLT Compression Force

As previously discussed, an analogy between the connection and a monolithic beam must be made in order to achieve member compatibility, thus allowing for the strain at a given connection rotation to be determined. By making this analogy between two identical walls, one with a hybrid connection and one with a fixed connection acting as a cantilever, the elastic displacements, Δ_e, are equal and thus, the displacement due to the connection rotation, Δ_{gap}, and the plastic deformation of the cantilever, Δ_p, must be equal [Ganey, 2015].

[Ganey, 2015] derived the compression strain for his research on CLT as:

$$\epsilon_w = \left(\frac{\theta_{imp} h_w}{l_p \left(h_w - \frac{l_p}{2} \right)} - \phi_e \right) c \tag{8}$$

Where

l_p = Plastic Hinge Length

ϕ_e = Elastic Curvature

$$\phi_e = \frac{M}{EI} \tag{9}$$

Alternatively, [Newcombe et al., 2008] proposed the following expression for his research on LVL:

$$\epsilon_w = \left(\frac{3\theta_{imp}}{L_{cant}} + \phi_{dec} \right) c \tag{10}$$

Where

L_{cant} = Shear Span or Effective Height of the Wall (approximately 67% of the total building height for a triangular force distribution)

ϕ_{dec} = Decompression Curvature

$$\phi_{dec} = \frac{M_{dec}}{EI} \tag{11}$$

Both [Newcombe, 2008] and [Marriott, 2009] had noticed that the effective modulus of the connection (E) was not equal to the parallel-to-grain modulus (E_{para}), and thus, due to the apparent end effects of the timber connection in compression, [Newcombe, 2008] proposed a reduced elastic

modulus for his LVL systems:

$$E = 0.55E_{para} \tag{12}$$

This reduced modulus is similar to the guidelines put forth by the Structural Timber Innovation Company based in New Zealand, $E = 0.7E_{para}$ [Structural Timber Innovation Company, 2013]. The modulus of elasticity used in this study will be obtained via laboratory material tests, while preliminary calculation will use the elastic modulus provided by the CLT manufacturer. By assuming a triangular stress distribution, the CLT compression force can be calculated as:

$$C_{CLT} = 0.5 f_{CLT} c b_w \tag{13}$$

Where

b_w = Wall Width

f_{CLT} = CLT Compression Stress as per Figure 2.9b

$$f_{CLT} = E\epsilon_w \leq f_y \tag{14}$$

5. Check Section Equilibrium

Vertical force equilibrium can be determined using the contributions from the weight of the wall, $F_{self-weight}$, PT force, T_{PT}, and the CLT compression force, C_{CLT}. If equilibrium is not satisfied, then the estimated neutral axis depth does not correspond with the chosen gap rotation. This process must be repeated, iterating the neutral axis depth, until equilibrium is achieved.

$$T_{PT} + F_{self-weight} = C_{CLT} \tag{15}$$

6. Evaluate Moment and Shear Capacity

Once equilibrium is satisfied, the connection moment can be determined. The moment arm of the connection, d_{con}, is the distance between the centroid of the section and the centroid of the compression stress, $\bar{c}$.

$$M_{con} = C_{CLT} d_{con} \tag{16}$$

Where

d_{con} = Connection Moment Arm

$$d = \frac{L_w}{2} - \bar{c} \tag{17}$$

The shear capacity is taken as the moment capacity divided by the height of the wall.

$$V = \frac{M_{con}}{h_w} \tag{18}$$

7. Determine Wall Displacement

The overall wall displacement can be determined by considering the rigid body motion due to the gap opening, δ_{gap}, and the elastic deformations, δ_e.

$$\delta_{tot} = \delta_{gap} + \delta_e \tag{19}$$

Where

$$\delta_{gap} = \theta_{imp} h_w \tag{20}$$

$$\delta_e = \frac{M_{con}}{k_w h_w} \tag{21}$$

2.5.2 The Winkler-Spring Model

Although the MBA is often used when analyzing concrete and masonry structures, providing a solution to the strain compatibility issues at the base of the wall, [Newcombe, 2011] outlines a few concerns regarding its use with post-tensioned timber walls. [Newcombe, 2015] summarizes these points as follows:

- The key assumption of the MBA is that the hybrid connection at the base of the wall can be represented by an equivalent monolithic connection. However, due to the large difference in the compressive stiffness, when compared to concrete and steel, the neutral axis depth for the timber wall is highly variable and thus, this assumption may not be accurate.
- it is inaccurate to assume that the shear span, L_{cant} of Equation 10, would have an effect on the strain in the base connection.
- The use of the effective connection modulus, E, and the shear span, L_{cant}, can result in an underestimate in the timber strain and thus, experience larger than expected levels of damage for a given design level.

As these issues were realized, the need for a new methodology emerged. Based on his previous works, [Newcombe, 2011] proposed the Winkler-Spring Analogy (WSA) design approach. As opposed to the MBA, the Winkler-Spring Analogy describes the behavior of the rocking wall base as a series of springs between the wall and foundation. An empirical relationship describes the effective length, L_{eff}, of the springs and is determined through analysis of the stress field in the rocking toe. Through finite element models and experimental analysis, [Newcombe, 2011] proposed the following empirical equation as a function of the neutral axis depth, c, and the length of the wall, l_w:

$$L_{eff,Winkler} = 120\left(\frac{l_w}{c} - 1\right) \tag{22}$$

Thus, equation 10, originally presented by [Newcombe et al., 2008], is updated to:

$$\epsilon_w = \frac{\theta_{con} c}{L_{eff}} \tag{23}$$

In comparison to the MBA, with regards to engineered timber the WSA produces a larger estimate of the stress in the base of the wall, based on this study by [Newcombe, 2011]. This is a result of the MBA essentially using a larger effective length. This will result in a reduced axial stiffness, which then results in the underestimate of stress when using the MBA approach on softer materials, such as timber products [Newcombe, 2015, Kovacs and Wiebe, 2017]. In addition, as previously outlined by [Kovacs and Wiebe, 2017], the WSA does not require any additional calibration from experimental data [Sarti, 2015]. This will prove beneficial when considering the widely varied nature of timber products. For these reasons, in this thesis the design analysis of Section 3.2 will be based on the Winkler-Spring Analogy design approach.

3 Structural Design and Analysis

This section presents the design and analysis of the controlled rocking CLT wall. First, the reference structure, to be located in Victoria, BC, will be designed. This three-storey structure follows the design requirements put forth in the National Building Code of Canada (NBCC), [NRCC, 2015], as well as the findings and proposed design parameters of recent researchers in the field of controlled rocking timber. The latter portion of this section discusses the laboratory scaling of the reference CLT wall, followed by the iterative moment-rotation analysis, presented in Section 2.5. The accuracy of the findings from previous research, and how they transfer to the use of CLT, will be discussed later in this thesis.

3.1 Prototype Design

The prototype structure is defined as a three-storey, normal-importance structure with a 40 m x 40 m footprint, located in Victoria, BC. Each storey is 3.32 m in height, with a total height of 9.96 m. The initial design phase of the prototype structure presented here follows the force-based design procedure of the NBCC, and will result in the required number of walls and the initial post-tensioning force, while limiting drift to the NBCC prescribed 2.5%.

3.1.1 Estimate the Natural Period, T_n

In order to determine the seismic demand on the lateral force resisting system, an estimate of the natural period is required. The NBCC provides empirical formulas to estimate the natural period, based heavily on previous research on steel and concrete structures. As investigated analytically and experimentally by [Sarti, 2015], and further confirmed by [Kovacs and Wiebe, 2017], these empirical formulas were found to be a significant underestimate in regards to timber structures.

For the structural design in this thesis, the NBCC period approximations are used as a starting point for design. Through an iterative process, varying the number of walls and initial PT force, a more accurate structural period was determined through both an MDOF modal analysis and SAP2000 [CSI, 2012].

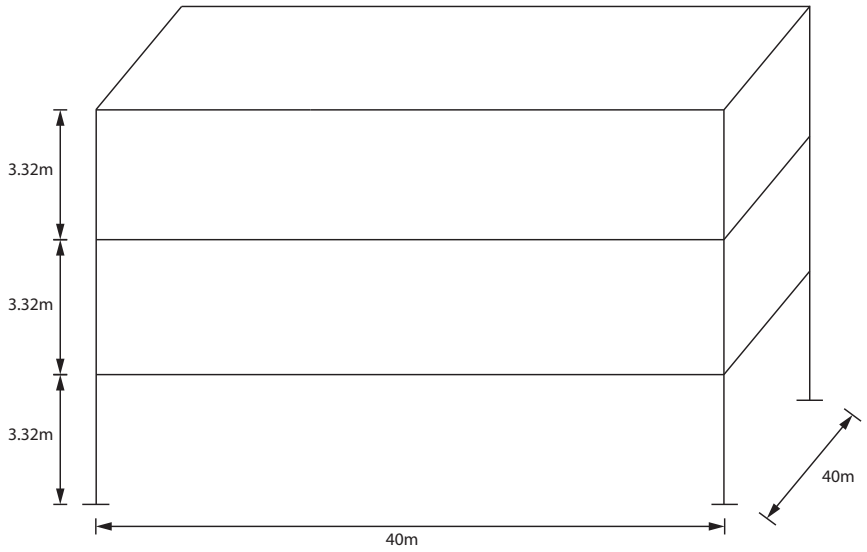

Figure 3.1: Prototype Structure

Table 3.1: Period Approximation

Area (m^2)	NBCC T_n (Cl.4.1.8.1) (s)	Modal Analysis T_n (s)
1600	0.28	0.413

3.1.2 Force Reduction Factor and Seismic Demand

The floor pressures and seismic weight used to calculate the seismic demand are shown in Table 3.2. In Canada, the force reduction factor, R_dR_o, is a two-part reduction factor that is applied during design to reduce the force that a specific structural element will see, in order to account for the expected non-linear displacement capacity of that structural element. This concept is depicted graphically by [Kovacs and Wiebe, 2017], in Figure 3.2. Recent findings from [Kovacs and Wiebe, 2017] suggest that an R_dR_o of approximately 8.0 to control roof drift to 2.5% is appropriate. Furthermore, an additional term, C_R, proposed by [Zhang et al., 2018], acts as a correction term for the non-linear displacement demand. C_R for the prototype structure is determined in Section 3.1.3.

To determine the seismic demand of the structure, a design base shear is determined and dis-

Table 3.2: Floor Pressures and Seismic Weight

Roof Pressures		Floor Pressures	
Dead Load kPa	Snow Load kPa	Dead Load kPa	Snow Load kPa
2.3	1.08	3.0	-
Seismic Weight			
Roof kN		Floor kN	
3680		4800	

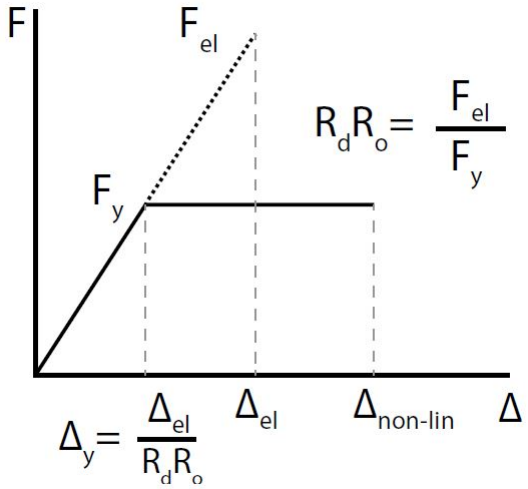

Figure 3.2: Canadian Force Reduction Factor for Rocking Response [Kovacs and Wiebe, 2017]

tributed to each storey of the structure. This distribution ultimately results in the individual storey shear forces and an overturning moment for the structure. The overturning moment is then used to determine the initial hold-down force on the rocking wall; for the purpose of this thesis, the hold-down force comes from the initial stressing of post-tensioning cables. The base shear is determined as follows, via the Building Code of Canada [NRCC, 2015]:

$$V_b = \frac{M_v I_E S_a(T) W_{trib}}{R_d R_o} \tag{24}$$

Where

M_v = Higher mode effects modifier

I_E = Building importance factor

$S_a(T)$ = Spectral acceleration

W_{trib} = tributary seismic weight

For timber rocking systems, the factor for higher mode effects is undefined, and thus M_v is taken as 1.0. Similarly, this thesis will consider a normal importance structure, making I_E equal to 1.0 as well. The spectral acceleration, $S_a(T)$, is a function of the natural period, T_n, and is determined using the seismic response spectrum of the structure's geographical location. Shown in Figure 3.3 is the response spectrum of Victoria, BC, for 5% damping.

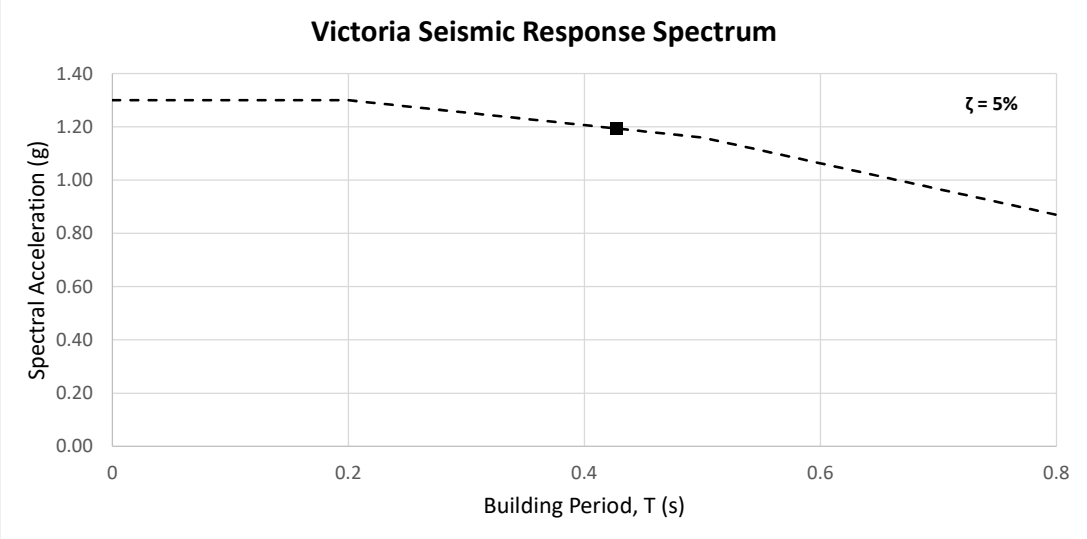

Figure 3.3: NBCC Response Spectrum for Victoria, BC

Lastly, the tributary seismic weight, W_{trib}, can be determined from Table 3.2, and an R_dR_o of 8.0 is used [Kovacs and Wiebe, 2017]. The overturning moment of each floor is then determined by distributing the base shear, V_b, to each storey. Shown in Table 3.3 is the base shear and overturning moment of the design.

Table 3.3: Base Shear and Overturning Moment

Base Shear, V_b *(kN)*	Overturning Moment, M_{OTM} *(kNm)*
1993	14859

3.1.3 Wall Configuration and Initial Post-Tensioning Force

The wall design used in this analysis is summarized in Table 3.4, with a total height of 9960 mm. An iterative process is then completed in order to determine the number of walls required, as well as the initial post-tensioning force required to resist the seismic demand on the structure. This process is comprised of cycling through the number of walls used in the structural design, determining the required post-tensioning force based on the number of walls chosen, and verifying that the design does not exceed 2.5% drift.

Table 3.4: Wall Design

Thickness, b_w (mm)	Length, L_w (mm)	Cross-Sectional Area (m^2)
320	4920	1.6

The non-linear correction term, C_R, is determined as follows:

$$C_R = \frac{\Delta_{nonlin}}{\Delta_{el}} = (R-1)^{0.515}\frac{0.184 + 0.199(1-\beta)^{1.173}}{T_1^{1.478}} + 1 \tag{25}$$

Where

β = Hysteretic energy dissipation parameter of flag-shaped hysteresis [Zhang et al., 2018]

The initial 5% damping coefficients were used in this calculation [Zhang et al., 2018]. A modified force reduction factor is used for the individual wall design in order to reduce the number of walls required, while still achieving an appropriate level of drift.

Table 3.5: Wall Configuration and Design Factors

T_n (s)	Modified Reduction Factor $R_d R_o$	Non-Linear Correction C_R	Number of Walls
0.413	4.44	3.12	12

The post-tensioning elements chosen for design are 15 mm strands with a yield strength of 1,670 MPa and a cross-section area of 140 mm^2, produced by DYWIDAG Canada [DYWIDAG-Systems International, 2015]. For the design used in this thesis, the PT elements will be located in the center of the wall. Due to a lack of guidance from research on quantifying long-term losses for the post-tensioning of CLT elements, these losses will be neglected from the analysis. However, past studies on timber walls constructed of other engineered wood products, by [Yeoh et al., 2012] [Morris et al., 2012], have shown that high levels of stress can result in long-term creep problems and thus, must be studied further [Kovacs and Wiebe, 2017].

An initial post-tensioning force is required to resist the overturning moment shown in Table 3.3. In order to do so, the connection forces at the base of the wall, as well as the overturning moment acting at the edge of the wall, must be considered. Once the wall begins to respond non-linearly, or when uplift occurs, the forces at the base of the wall are then defined by stress conditions, as opposed to static forces [Kovacs and Wiebe, 2017]. For the initial design in this thesis, a linear strain profile is assumed for the rocking toe of the CLT wall and thus, it is assumed that the rocking toe will exhibit an elastic material behaviour. This linear profile, depicted in Figure 3.4, can be simplified to a single compressive point load acting at one third of the distance from the rocking toe. The strain profile is bound by a neutral axis, c, in which [Sarti, 2015] suggests that rocking will begin when the neutral axis is at the center of the wall. However, [Sarti, 2015] recommends a neutral axis depth of 30% of the wall length for the analysis of a wall with post-tensioning at its center. In order to determine the location of the neutral axis after rocking has begun, an iterative process must be conducted, as discussed in Section 2.5.

Thus, in taking the moment about the rocking toe, for the design considered in this thesis, the

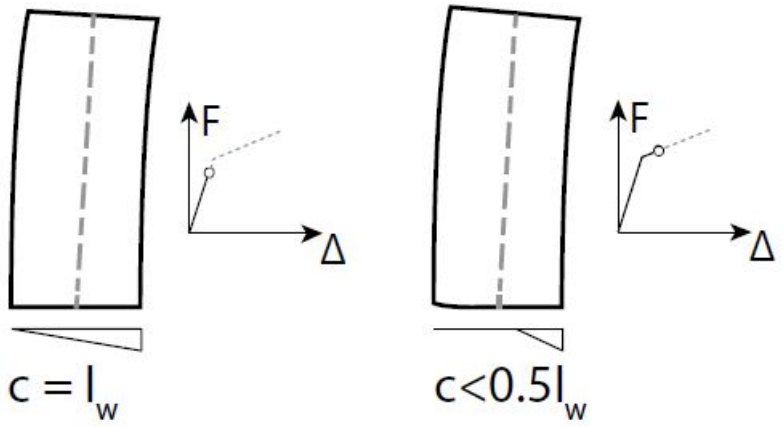

Figure 3.4: Linear Stress Profile at the Rocking Toe, as suggested by [Sarti, 2015]

following equation is obtained.

$$M_{con,design} = F_{self-weight}\frac{L_w}{2} + T_{PT,initial}\frac{L_w}{2} - C_{CLT}\frac{c}{3} \tag{26}$$

Where

$F_{self-weight}$ = Wall Weight

$T_{PT,initial}$ = Initial Post-Tensioning Force

L_w = Wall Length

C_{CLT} = Compressive Force = $F_{self-weight} + T_{PT,initial}$

Solving for the initial post-tensioning force:

$$T_{PT,initial} = \frac{M_{con,design} - F_{self-weight}(\frac{L_w}{2} - \frac{c}{3})}{\frac{L_w}{2} - \frac{c}{3}} \tag{27}$$

Using the input parameters above, the initial post-tensioning force is 1100kN.

3.1.4 Non-Linear Displacement

In order to confirm the initial design, the maximum non-linear deflection must be determined and verified with the maximum 2.5% drift limit outlined in the NBCC [NRCC, 2015]. In order to do so, the elastic deflection is multiplied by the force reductions factors, $R_d R_o$, and the correction term, C_R, proposed by [Zhang et al., 2018]. For a general loading case, bending and shear deflections are calculated as:

$$\delta_b = \int \int \frac{M(h)}{EI} dh \tag{28}$$

$$\delta_s = \int \int \frac{V(h)}{G_{CLT} A_v} \tag{29}$$

[Sarti, 2015] proposed a simplified derivation for displacement assuming the prototype structure is designed with both storey heights and weights being equal. These equations allow for the calculation of the total elastic deflection as a function of the design connection moment, $M_{con,design}$, inter-storey height, H, and the CLT wall material properties. These equations are derived under the simplifying assumption of an inverted triangular distribution of the earthquake loading [Sarti, 2015, Kovacs and Wiebe, 2017].

$$\delta_b = \frac{M_{con,design} H^2}{6 E_{CLT} I_Z} \frac{n}{\sum_{i=1}^{n} i^2} \sum_{i=1}^{n} i^3 (3 - \frac{i}{n}) \tag{30}$$

$$\delta_s = \frac{M_{con,design}}{G_{CLT} A_v} \tag{31}$$

Where

n = Number of Storeys

A_v = Shear Area

G_{CLT} = CLT Shear Modulus Approximation [Ganey, 2015]

$$G_{CLT} = \frac{E_{CLT}}{16} \tag{32}$$

The total elastic deflection is the sum of the flexural and shear deflections:

$$\delta_e = \delta_b + \delta_s \tag{33}$$

By multiplying by the force reduction factors, $R_d R_o$, and the correction term, C_R, the maximum non-linear deflection is obtained:

$$\delta_{non-linear} = (\delta_b + \delta_s) R_d R_o C_R \tag{34}$$

The maximum non-linear deflection is given in Table 3.6. Note that $R_d R_o$ here is based on the designed wall strength, including overstrength, rather than the $R_d R_o$ used to determine the minimum design forces.

Table 3.6: Maximum Non-Linear Deflection

Modified Reduction Factor $R_d R_o$	Non-Linear Correction C_R	Non-Linear Deflection (mm)	Drift (%)
4.44	3.12	248	2.49

3.1.5 Initial Design Summary

A controlled rocking CLT wall was considered for the initial design of a three-storey, normal-importance structure located in Victoria, BC. Following the force-based design procedure outlined in the NBCC, the seismic overturning moment demand on the structure was determined and used

in the design of each CLT wall. For the design, the maximum non-linear displacement was limited to 2.5%, as prescribed by the NBCC. The initial design parameters are shown in Table 3.7.

Table 3.7: Initial Design Summary

Area	1572	m^2
Period, T_n	0.413	s
Overturning Moment, M_{OTM}	14859	kNm
Modified Reduction Factor	4.44	$R_d R_o$
Non-Linear Correction	3.12	C_R
Number of Walls	12	
Design Moment, $M_{con,design}$	2233	kNm
Non-Linear Deflection	248	mm
$T_{PT,initial}$	1100	kN
Axial Stress	0.699	MPa

3.2 Experimental Design Analysis

This section outlines the analysis of the controlled rocking wall by following the iterative moment-rotation analysis outlined in Section 2.5, Figure 2.10, and utilizing the Winkler Spring Analogy, as discussed in Section 2.5.2. As further discussed in Section 2.5.2, the Winkler Spring Analogy provides a connection stiffness through an empirical relationship between the neutral access depth, c, and the base rotation, θ_{con}.

The response of the base connection of the wall was analyzed at discrete points, from a base rotation of 0% to 5%. The result of the analysis will be a pushover plot, shown in Section 3.3.

It should be noted again that this design and analysis does not incorporate any additional energy dissipation devices so as to simplify the interpretation of experimental results, given that the focus was intended to be on the behaviour of the wall-foundation interface rather than on the behaviour of the overall system. Therefore, the energy dissipation, β, is taken as 0.

3.2.1 Laboratory Scaling and Parametric Study

Due to laboratory space constraints, full-scale specimen testing was not feasible. Therefore, the experimental tests were conducted on one-half scale specimens. The scaled CLT wall parameters are shown in Table 3.8. Scaling effects on CLT are not considered in this research and must be further studied.

Table 3.8: Experimental Half-Scale Walls

	h_w (mm)	l_w (mm)	b_w (mm)	$T_{PT,initial}$ (kN)
Full-Scale	9960	4920	320	1100
Half-Scale	4980	2460	160	275

In order to gain a better understanding of the behaviour of CLT in a controlled rocking context, a parametric study was planned. The study included varying different design aspects of the CLT panel and their effect on the rocking behaviour. A second wall, 3-ply and narrower width, 1600 mm, was tested and will be discussed with the results of this study.

3.2.2 Base Strain Profile and Assume Connection Rotation

A key aspect of this thesis is the investigation of the base strain profile of a CLT rocking wall. As discussed in Section 3.1.3, for this pre-experimental analysis, an elastic material behaviour is assumed, Figure 3.4. As the outcome of this analysis is a pushover plot, the total roof drift must be determined. As discussed by [Newcombe, 2011, Kovacs and Wiebe, 2017], timber rocking walls must consider both flexural and shear deformations, in addition to the displacement due to the connection rotation when considering total roof drift, Figure 3.5. In order to obtain these deformations, a connection rotation, θ_{con}, must be assumed. As the elastic deformations are dependent on the connection rotation, an additional level of iteration is required.

For the following analysis explanation, θ_{con} of 0.015 radians will be used. It will be shown in Section 3.2.8 that this connection rotation targets a total roof drift of 0.019 radians.

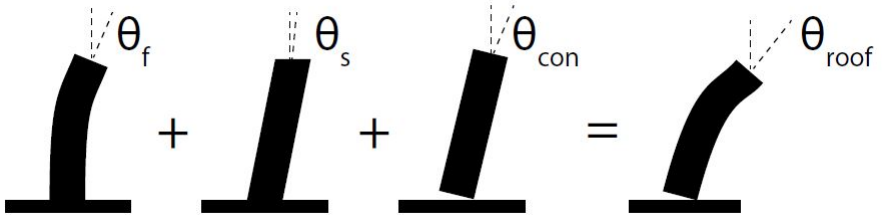

Figure 3.5: Roof Drift Contributions [Kovacs and Wiebe, 2017]

3.2.3 Neutral Axis Depth and Winkler Spring Analogy

An initial assumption of the neutral axis depth is made, and the Winkler spring length is determined using Equation 22, [Newcombe, 2011]. For a connection rotation of 0.015 radians, a neutral axis depth of 364.7 mm was solved for, discussed in Section 3.2.6, with an associated spring length of 689.4 mm.

3.2.4 Rocking Toe Interface and Compression Force

The strain at the base of the wall is calculated using Equation 23. At a base rotation of 0.015 radians, the strain in the rocking toe is 0.079. The yield strain, which occurs at c_{yield}, is determined by dividing the yield strength of the CLT by the elastic modulus, E_{CLT}. For this study, the yield strength is taken as the CLT's compressive strength [Kovacs and Wiebe, 2017]. The yield strain of the laboratory prototype is 0.0087. Refer to Appendix A for material test data.

The compression force in the rocking toe is determined as follows:

$$C_{CLT} = b_w \int_0^c f_{CLT}(y)dy \tag{35}$$

If a bi-linear stress-strain relationship is assumed for the rocking toe [Kovacs and Wiebe, 2017], then the compression force can be simplified as:

$$C_{CLT} = 0.5 f_{CLT} c b_w, c \leq c_{yield} \tag{36}$$

$$C_{CLT} = b_w \left[\sigma_y \frac{c_{yield}}{2} + \sigma_y (c - c_{yield}) \right], c \geq c_{yield} \tag{37}$$

As summarized by [Kovacs and Wiebe, 2017], the analysis procedure conducted by [Sarti, 2015] assumes that that the rocking toe does not experience any non-linearity, even at larger roof drifts. This is due to the use of the MBA, as opposed to the WSA used by [Kovacs and Wiebe, 2017] and herein. And thus, the MBA produces an underestimate of strain, due to the use of a longer effective spring length [Kovacs and Wiebe, 2017, Newcombe, 2011]. [Kovacs and Wiebe, 2017] further recommended that Equation 22 be investigated for CLT, as it was initially developed for the analysis of LVL panels.

The compression force at 0.015 radians is 558 kN.

3.2.5 Post-Tensioning Force

The initial post-tensioning force, $T_{PT,initial}$, was determined in Section 3.1.3, in order to produce a connection moment that would resist the over-turning moment. As the wall begins to uplift, the tension force in the post-tensioning elements begins to increase. [Newcombe, 2011] and [Sarti, 2015] had suggested that this change in force be determined using the vertical component of the element elongation however, a discussed by [Kovacs and Wiebe, 2017], this simplification can result in underestimate of the force, especially as the base rotation increases. In addition to the vertical elongation component, [Kovacs and Wiebe, 2017] proposed the following equations to include the horizontal component of the post-tensioning elongation, as well as wall shortening due to relaxation:

$$\Delta x_{PT} = \theta_{roofdrift} h_w \tag{38}$$

$$\Delta_{CLT,relax} = \frac{T_{PT,initial} + F_{SW}}{b_w L_w E_{CLT}} h_w \tag{39}$$

For the purpose of predicting the laboratory tests, the inclusion of CLT relaxation will be neglected. The force that results from the total elongation is then add to the initial post-tensioning force.

The post-tensioning force at 0.015 radians is 549 kN, which results in an axial stress of 1.4 MPa.

3.2.6 Check Force Equilibrium

The compression force, post-tensioning force, and self-weight of the wall are then used to check equilibrium using Equation 15. If equilibrium is not satisfied, the previous steps, Sections 3.2.2-3.2.5, must be re-iterated until equilibrium is achieved and the correct neutral axis depth in obtained. These iteration can be easily completed for multiple levels of base rotation in a spreadsheet.

3.2.7 Determine Connection Moment

Upon achieving force equilibrium, the resulting moment during the elastic phase of rocking is determined by taking moments about the rocking toe, Equation 26. During the non-linear stage of rocking, the moment about the rocking toe is taken as:

$$M_{con,design} = F_{self-weight}\left(\frac{\theta_{con}h_w}{2}\right) + T_{PT}\left(\frac{L_w}{2}\right) - C_{CLT}\left(\frac{c - c_{yield}}{2} + \frac{c_{yield}}{3}\right) \tag{40}$$

At a base rotation of 0.015 radians, the CLT wall is still in the elastic rocking stage, with a resisting moment of 608 kNm.

3.2.8 Determine Total Roof Displacement

Although the base rotation will have the largest contribution to the total roof drift, it is expected that the elastic deformations will have a relatively significant contribution as timber is considered a flexible material, shown in Figure 3.5. The elastic deformations are determined as follows:

$$\Delta_e = \frac{M_{con}}{k_w h_w} \tag{41}$$

Where

k_w = CLT Wall Stiffness

$$k_w = \left(\frac{h_w^3}{3E_{CLT}I_w} + \frac{h_w}{G_{CLT}b_w L_w} \right)^{-1} \tag{42}$$

The total roof drift is then calculated as:

$$\theta_{total} = \frac{\Delta_e}{h_w} + \theta_{con} \tag{43}$$

$$\Delta_{total} = \theta_{total} h_w \tag{44}$$

At a base rotation of 0.015 radians, the total roof drift is 0.019 radians (95 mm).

3.2.9 Axial Stress Comparison

By using axial stress as a point of comparison to previous literature, the appropriateness of the design procedure can be determined. Table 3.9 depicts the theoretical axial stress, in N/mm^2, at each level of drift from various studies, including [Kovacs and Wiebe, 2017], [Sarti, 2015], [Newcombe, 2011] and [Ganey, 2015]. Using the data presented in these studies, the axial stress at each level of drift was calculated by dividing the peak post-tensioning force at the given level of drift, by the cross-sectional area of the wall. Since each study references different design standards and codes, there is a large variance when looking at the data from [Sarti, 2015] and [Newcombe, 2011]. However, when comparing to [Ganey, 2015], whose design process mirrors that of this study, it can be concluded that the approximate design procedure is appropriate.

Table 3.9: Axial Stress Comparison to Literature (MPa)

Literature	**Ficara**	Kovacs	Sarti 1	Sarti 2	Newcombe 1	Newcombe 2	Newcombe 3	Ganey 1	Ganey 2
0.00	**0.70**	0.22	1.34	2.01	0.5	0.592	0.592	0.852	0.478
0.005	**0.90**	-	1.76	2.35	0.626	0.724	0.724	-	-
0.01	**1.14**	-	2.26	2.85	0.688	0.894	0.894	1.28	0.957
0.015	**1.40**	-	2.77	3.32	-	1.052	1.092	-	
0.02	**1.65**	0.55	-	-	0.938	1.25	1.288	1.7	1.383
0.025	**1.91**	-	-	-	-	-	-	-	-
0.03	**2.17**	-	-	-	1.188	-	-	2.13	2.129

3.3 Preliminary Model Result

The preliminary model results for Wall 1, based on the analysis process described in Section 3.2, are shown in Figure 3.6. This model is based on material test data, shown in Appendix A. The measured modulus of elasticity was only 37% of the manufacturer's recommended value, although the manufacturer had also identified that recommendation as only preliminary because the provided product was so new at the time.

E_w = 2409 MPa

G_w = 151 MPa

k_i = 5877 kN/mm

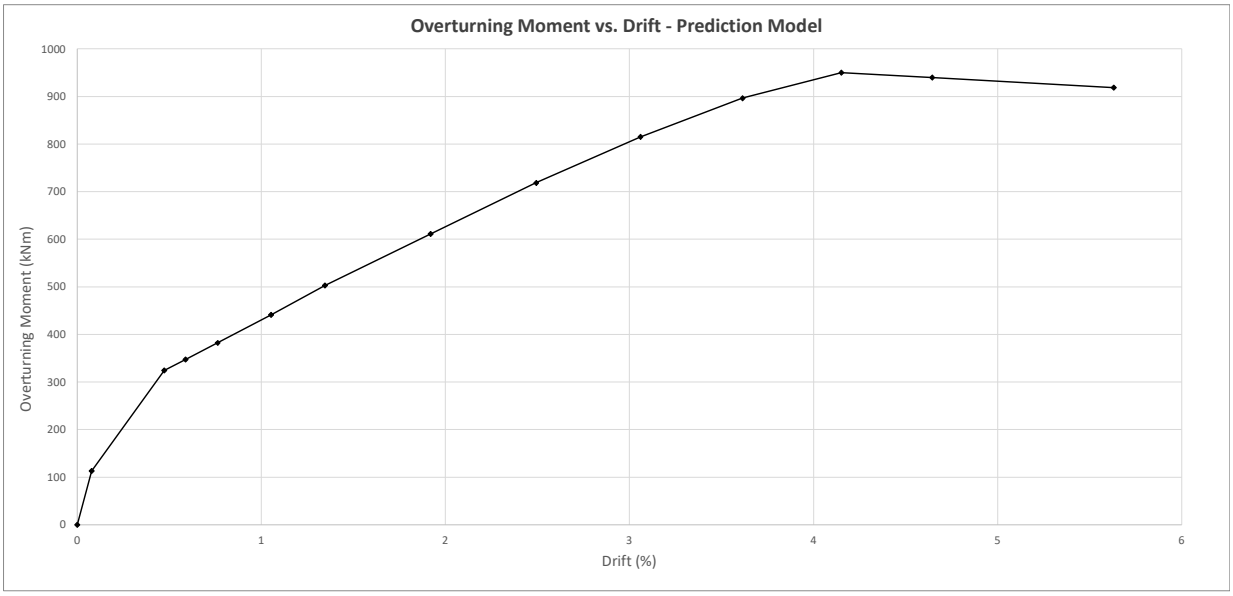

Figure 3.6: Overturning Moment vs. Drift for Wall 1 from Prediction Model

4 Experimental Setup

This section outlines the laboratory design and instrumentation setup, as well as the testing method performed in this study. Two prefabricated half-scale CLT walls were subjected to quasi-static reverse cyclic loading protocols. The panels varied in width and thickness, however, the axial stress at each level of drift was held constant. The tests were conducted at the Applied Dynamics Laboratory at McMaster University in Hamilton, Ontario.

4.1 CLT Panels

The CLT panels, shown in Figure 4.1, used in this study were constructed by Element5 Co. [Element5, 2019], a Canadian company based in Quebec. The panels used were European grade C24 from Austria. Material tests on small specimens was conducted at McMaster University. This data can be found in Appendix A, and was used to update the assumed material property values used in the prediction models discussed in Section 3. The updated prediction model is later discussed in Section 6.2. Table 4.1 shows the physical properties of each panel.

Figure 4.1: CLT Panel Manufactured by [Element5, 2019]

Table 4.1: CLT Panel Physical Properties

	Height (mm)	Width (mm)	Thickness (mm)	# of Plies
Wall 1	4980	2460	160	5
Wall 2	4980	1600	96	3

4.2 Rocking Wall Test Details

4.2.1 Test Setup

The tests were conducted on an existing reinforced concrete slab, previously secured to the strong floor using 2.5-3" diameter, post-tensioned steel bolts spaced at 3' intervals. Wall 2 was the first panel to be tested. During the test, it was observed at the concrete slab surface was not perfectly smooth and level. Therefore, to ensure a relatively smooth and level surface for the second test on Wall 1, a layer of Hydro-Stone was applied to the top of the slab. The CLT wall stood on the slab and was braced laterally using uni-axial rubber rollers that would adjust to the wall thickness as needed. In order to allow rocking, while preventing sliding, shear keys were installed on the slab, shown in Figure 4.2.

4.2.2 Lateral Loading System and Loading Protocol

The quasi-static reverse cyclic loading protocol was achieved using an MTS hydraulic actuator. The actuator has a capacity of 500 kN in both directions, and a total stroke of 500 mm. In order to cycle the wall in both directions, the actuator was centered at half-stroke, allowing for a maximum stroke of 250 mm, or 5% of the wall height, in each direction.

In order for the wall to rock, the actuator needed to be able to rotate in the vertical direction. This was achieved through the use of chain blocks. Additionally, for the actuator to transfer the total load to the wall evenly, the actuator needed to be mounted to a strong reaction frame. The actuator was mounted to columns using high strength steel rods and was braced to McMaster University 'Frankenstein' frame, to resist horizontal motion, and connected to the wall through a strong loading beam that would be fixed to the wall, see Figure 4.3. The loading beam was constructed using angle sections welded to a steel plate that were the length of the wall. The angles would provide stiffness

Figure 4.2: Shear Key

to the loading beam, as well as provide a socket for the wall to be attached. Holes were drilled into the angle sections and the top of the CLT panel. High strength, threaded steel rods were inserted and bolted to provide a fixed connection to the wall. Stiffeners were then welded to the angles for added safety.

Similarly to the study conducted by Ryan Ganey, [Ganey, 2015], the loading protocol used for this study was developed using ACI ITG-5.1-07 'Acceptance Criteria for Special Unbonded Post-Tensioned Precast Structural Walls Based on Validation Testing' [ACI, 2007]. The loading protocol is shown in Table 4.2. For each stage of loading, both the loading rate and axial force would increase simultaneously. As the CLT panel would reach the maximum drift at each cycle, the test was paused to make observations, and then resumed.

(a) Wall Insertion Side

(b) Actuator Connection Side

Figure 4.3: Loading Beam Design

4.2.3 Axial Loading System

Hydraulic actuators were used to apply a constant axial force to the system during each cycle. This was mainly due to the fact that the laboratory did not have the means to post tension tendons of this magnitude, and it was not feasible to hire an outside contractor for such a limited scope of work. A benefit of this approach to providing axial loading was that the load could be well controlled and monitored at all stages of testing.

The axial force, as shown in Table 4.2, was held constant for each cycle at the theoretical maximum force the tendons would experience at the given level of drift, and starting with an initial tension force of 275 kN. Four 250 kN hydraulic actuators, two on either side of the wall as shown in Figure 4.4, were used to achieve this axial load. Due to the stiffness of the loading beam, as well as the proximity to each other, the analysis presented in this paper conservatively assumes loading in the center of the wall. In addition, beyond cycle 10 of the loading protocol, the axial force was held constant at 800 kN, as this was the theoretical yield point of the post-tensioning tendons assumed for the original structure design.

In order to distribute the load from the actuators to the loading beam evenly, two HSS sections sitting on rollers allowed for simple load transfer during the rocking motion, while also avoiding damage to the threaded rods. Due to the height of the test, high strength couplers were made

Table 4.2: Loading Protocol for Main Wall Test

Cycle No.	Target Drift (%)	Displacement (mm)	Target Axial Force (kN)	Loading Rate (mm/min)
1	0	0	0	-
	0	0	275	-
2	0.25	12.5	310	1.5
	-0.25	-12.5	310	1.5
3	0.35	17.5	327	2.5
	-0.35	-17.5	327	2.5
4	0.5	25	355	3.6
	-0.5	-25	355	3.6
5	0.75	37.5	405	5.4
	-0.75	-37.5	405	5.4
6	1	50	458	7.1
	-1	-50	458	7.1
7	1.5	75	549	10.7
	-1.5	-75	549	10.7
8	2	100	651	14.3
	-2	-100	651	14.3
9	2.5	125	752	17.85
	-2.5	-125	752	17.85
10	3	150	800	21.4
	-3	-150	800	21.4
11	4	200	800	28.5
	-4	-200	800	28.5
12	5	250	800	35.6
	-5	-250	800	35.6

in-house in order to achieve the desired length of threaded rod.

(a) 250kN Capacity Actuators at Base of the Wall

(b) Threaded Tensioning Rods Connecting Actuator to Loading Beam

Figure 4.4: Axial Loading System

4.3 Instrumentation Plan

The instrumentation used in this study is shown in Figure 4.5.

The axial load on the wall was controlled by two 500 kN load cells, mounting below each of the the axial force transfer beams. Since a single hydraulic pump was used for the four axial actuators, only one load cell acted as a control. However, both load cells were never more than +/- 5 kN apart in measurement.

Lateral displacement of the wall was measured using a string potentiometer attached to the top of the wall, at 4980mm, and a rigid aluminum column. Readings from this potentiometer were used as a control value for the rocking cycles, as opposed to the actuator stroke, in order to avoid any internal displacements.

A line of six string potentiometers (S1-S6) along the base of the wall measured uplift and are used to determine the strain profile of the base of the wall. A rotary variable differential transformer

(RVDT) was centered at the base to measure the angular displacement and rigid body motion of the wall during rocking. In addition, four more string potentiometers were mounted diagonally to measure the shear deformations along the height of the wall.

In order to provide an appropriate comparison to the prediction model results, presented in Section 3.3, an understanding of the strain profile and distribution at the base of a CLT rocking wall was required. To capture this behaviour, six stain gauge rosettes were adhered to the wall at the location of the S1 through S6. Prior to the application of the rosettes, a study was performed to determine the optimal adhesion method, as strain gauges can be challenging to mount on timber. It was found that simply gluing the gauges, after a quick sanding and cleaning of the CLT surface, as one normally would, provided the clearest result. In addition to the rosettes, three strain gauges were mounted vertically on either end of the wall at 100 mm intervals to determine the height of the strain distribution at the rocking toe. In addition to comparing these results with the prediction models, digital image correlation method was also utilized in hopes to gather information on the entire strain profile, or map, of the rocking toe.

Figure 4.5: CLT Panel Instrumentation

4.4 Digital Image Correlation

During this study, data was gathered via digital image capturing. Although this data is not presented within this thesis because of limitations in the time available for data processing, it is included in the digital data record from the tests. This section outlines the data collection method as it pertains to the test setup and instrumentation.

Digital image correlation (DIC) is a non-contact method of taking measurements based on changes in the pixels of digital photos. This method has been successful in measuring both displacements and strains on three-dimensional objects and surfaces. Due to the non-contact nature, and large area coverage, DIC has the potential to be used in a wide variety of structure static and

dynamic testing.

Although the area being measured with DIC is a flat, two-dimensional, surface, the timber deflections and failure methods may be three-dimensional. In order to capture the three-dimensional characteristics, two digital SLR cameras were set up facing the wall's surfaces at different angles. Refer to Figure 4.6 for the DIC setup. In order for the DIC analysis programs to perform their analysis, there must be reference points within the digital image. The rocking toe of the wall was painted white, with a random speckled black dot pattern on top. The corners of the analysis region was marked with crosses. The DIC analysis program will recognize the crosses as the extents of the analysis region, while reading the pixel movements in the speckle pattern to measure the displacements and strains. Both cameras were wired to a single shutter button to ensure photos were taken simultaneously.

Figure 4.6: Digital Image Correlation Setup

5 Experimental Data Analysis and Observations

This chapter presents and discusses the experimental results as interpreted from the collected data. Observations made during the testing procedure that coincide with the collected data are also discussed. This chapter concludes with a comparison to the prediction model that was presented in Section 3.3.

5.1 Experimental Observations

5.1.1 Wall 1 Observations

The first visible uplift of Wall 1 was observed during the fourth loading cycle (0.75% drift), as shown in Figure 5.1, even though the data presented later indicate that only 30% of the wall base was in compression during the first loading cycle. At 1.5% drift, noticeable damage at the toe of the wall began, Figure 5.2. At this point of the test, the wall began to make noticeable creaking noises, along with the compression splitting shown in Figure 5.2 and minor delamination. After the 1.5% loading cycle, the test had to be stopped as the DIC camera batteries had to be replaced. During this pause, it became apparent that the post-tensioning connection at the base of the wall began to yield. Shown in Figure 5.3 is the horizontal steel plate that the axial load actuators are attached to. This image shows that the horizontal plate is yielding between the axial actuator and the connection to the base. To avoid any potential issues with the axial loading system, the test was put on hold so that the base connections could be reinforced. When the experimental procedure continued, the 1.5% and 2.0% drift cycles were repeated.

At 2% drift, the compression cracking began to widen and continue along the base of the wall; small pieces of timber began to splinter off due to the contact with the shear key, Figure 5.4. After the 3.0% loading cycle, noticeable permanent damage was observed in the rocking toes at zero lateral load, Figure 5.5.

Figure 5.1: Uplift at -0.75% drift

Figure 5.2: Compression Toe at 1.5% Drift

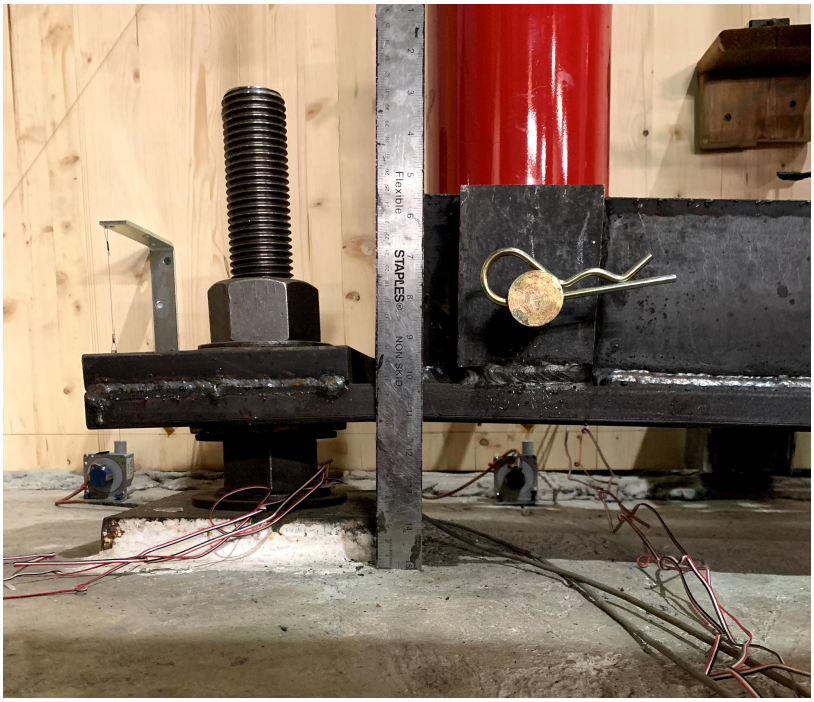

Figure 5.3: Yielding of Axial Connection at Base

Figure 5.4: Decompression Toe at 2% Drift

Figure 5.5: Permanent Damage to Rocking Toe after 3.0% Drift Cycle

Upon completion of the experimental procedure, compression cracks and delamination was noticeable within 500 mm from the edge of the wall with the splitting extending 200 mm up the height of the wall, Figure 5.6. However, when examining the base of the wall, it is clear that the majority of the damage was concentrated on the outer-most layers of the CLT, Figure 5.7, and thus, complete replacement may not be necessary in this situation.

Figure 5.6: Decompression Toe at 4% Drift

Figure 5.7: Post-Experimental Observation of Wall Base

5.1.2 Wall 2 Observations

During the wall 2 test, cracking and cracking-sounds were noticeable during the initial rocking stages, shown in Figure 5.8. During the 0.5% drift cycle, noticeable uplift was observed, as shown in Figure 5.9. Toe crushing was evident after the 2.5% drift cycle.

Figure 5.8: Initial Cracking at 0.35% Drift

Figure 5.9: Uplift at -0.5% Drift

At the 2.0% drift cycle, it was apparent that there was an issue due to the sound coming from

both the wall and the axial force actuators. The issue turned out to be the axial load distribution beam falling out of place, causing an uneven and out-of-plane force on the wall. At the point, the test was stopped and action was taken to correct the issue. Shown in Figure 5.10 is the axial load distribution beam during the 2.0% drift cycle.

Figure 5.10: Axial Load Distribution Beam during 2.0% Drift Cycle

The test was briefly paused so that the axial load distribution beam could be re-centered. The 3-ply panel was able to reach 3.0% drift before ultimately failing in out-of-plane buckling. At 3.0% drift, the maximum uplift of the rocking toe was significantly less than that of the 5-ply wall at 2.0%, shown in Figure 5.11. This was due to the significant damage that the 3-ply panel experienced.

As previously mentioned, the ultimate failure mode for the 3-ply wall was out-of-plane buckling, shown in Figure 5.12. This failure mode may have occurred due to the issues with the axial load

Figure 5.11: Decompression Toe at 3.0% Drift

distribution beam, off-centring and/or calibration issue with the axial loading system, and the slenderness of the panel itself. As a 3-ply panel will not likely be used for the loading scenario replicated in this study, and inter-storey connections will provide a larger out-of-plane load resistance, this failure method is the least concerning when it comes to rocking CLT panels.

Figure 5.12: Out-of-Plain Buckling Wall Failure

5.2 Data Analysis

5.2.1 Axial Force Calibration

Since actual post-tensioning tendons were not used in this study, it was important to track the behaviour of the load cells providing the axial load to the wall. If the system did not provide equal force to both sides of the wall, in all four actuators, the test would have to be shut down immediately for safety concerns. Shown in Figure 5.13 is the load data from both load cells at the top of the wall. Calibration was conducted in order to ensure the load was distributed evenly, and Figure 5.13 shows that the actuators provided constant simulated post-tensioning force as intended. Note that the intermediate data points at zero drift are readings taken while the wall is stationary and the axial load is increasing.

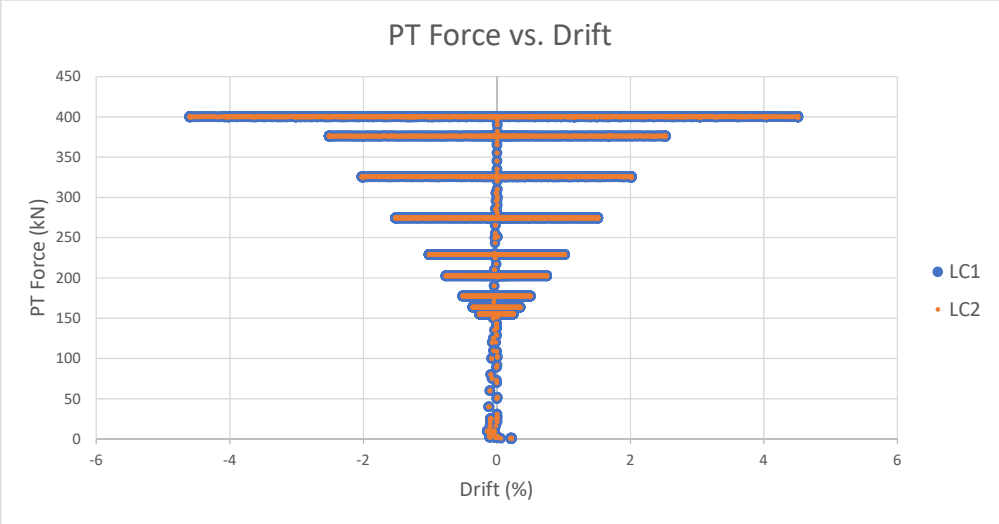

(a) Axial Force Load Cell Readings for Wall 1

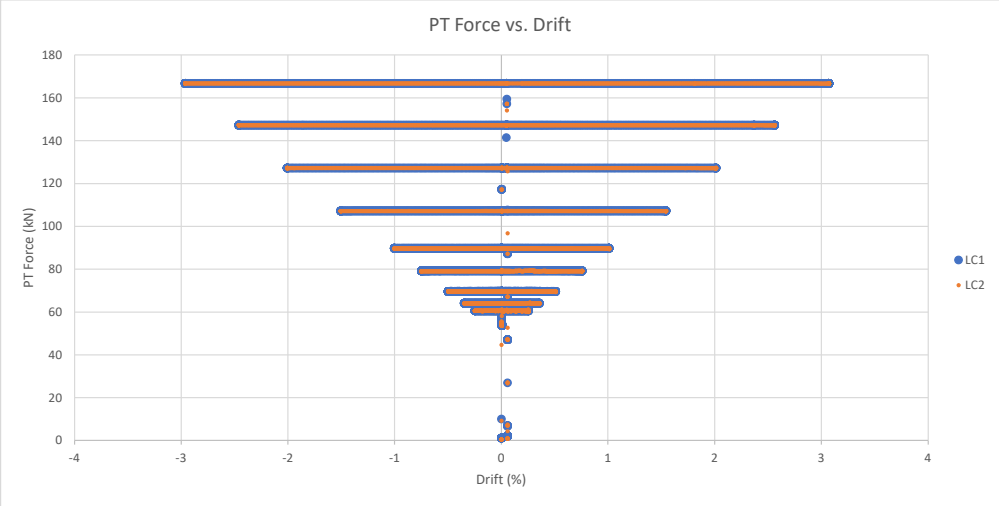

(b) Axial Force Load Cell Readings for Wall 2

Figure 5.13: Load Cell Data

5.2.2 Hysteretic Behaviour

The wall drift was determined using the string potentiometer that measured lateral displacement at the top of the wall, divided by the height at which it was measuring. The overturning moment was the applied lateral load multiplied by the height of the load cell. The plots of maximum overturning moment versus drift are shown in Figure 5.14 and Figure 5.15. The plotted moment is measured at the instant of peak drift achieved during the loading phase. This data is later compared to the prediction models in Chapter 6. For Wall 1, testing was terminated when the actuator stroke was reached, while for Wall 2, the testing was terminated after loading to 3% drift because of out-of-plane buckling, as discussed in Section 5.1.2. For Wall 1, in the positive pulling direction, a peak overturning moment of 850 kN was achieved, while in the negative pushing direction, a peak overturning moment of 927 kN was achieved. This difference is most likely the result of the different degrees of damage in each rocking toe, which also may vary due to the variability of natural products. Conversely, the peak strength was similar in both directions for Wall 2.

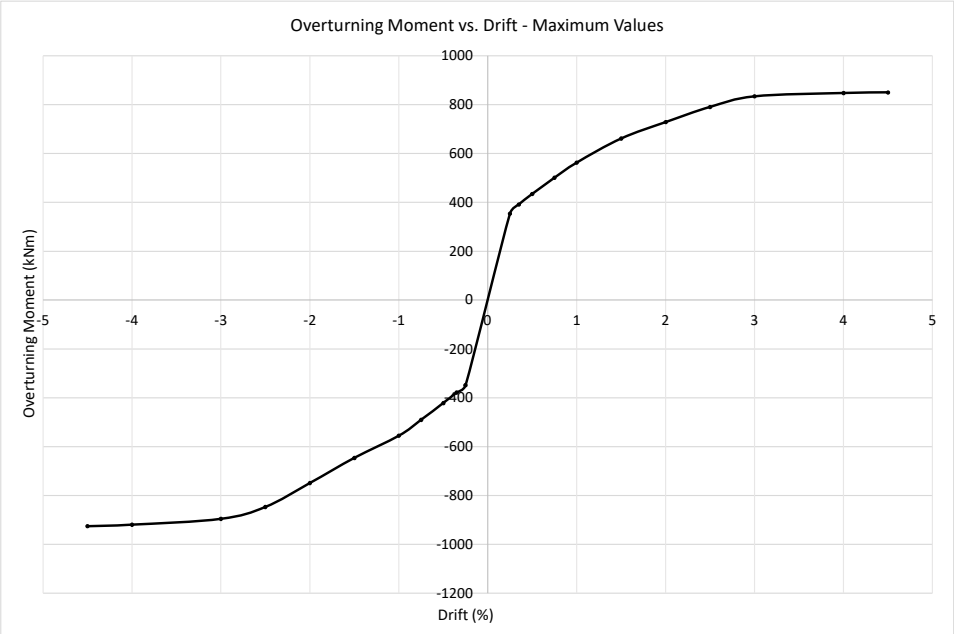

Figure 5.14: Maximum Values for Overturning Moment vs. Drift for Wall 1

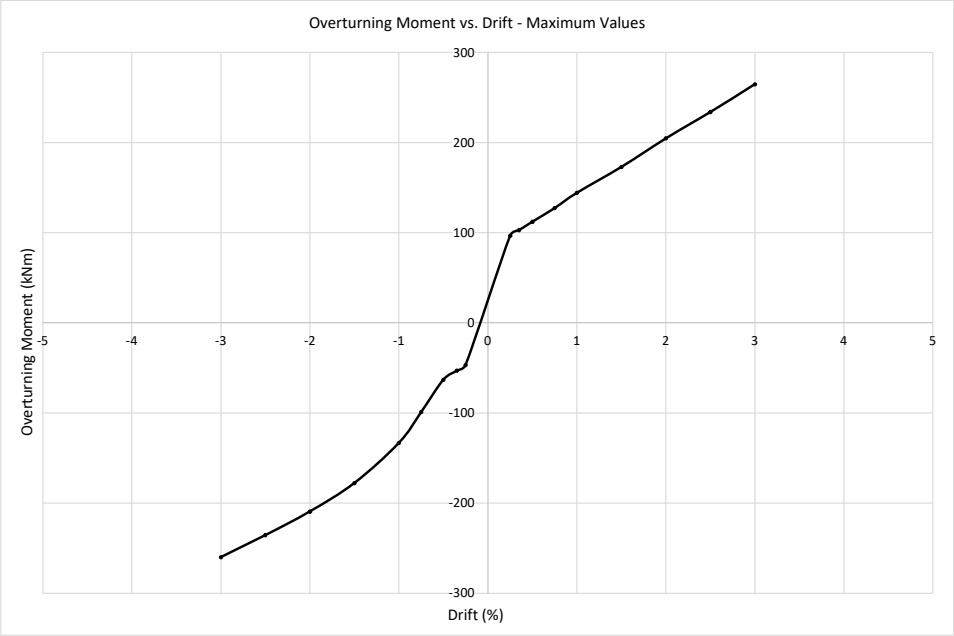

Figure 5.15: Maximum Values for Overturning Moment vs. Drift for Wall 2

Wall 1 was a 5-ply planel with a width of 2490mm, compared to wall 2 which was a 3-ply panel and 1600mm wide. Due to its smaller size, it is to be expected that wall 2 will not achieve large overturning moments. Additionally, as can be seen in Figure 5.15, there is a minor decrease in stiffness between 0 and 1% drift that occurs only in the negative pushing direction. There are many factors that could have caused this anomaly in the negative actuator pushing direction such as:

- Uneven rocking interface. For wall 2, the wall rested directly on the concrete slab, as opposed to a Hydro-Stone base as was used for Wall 1. The minor inconsistencies in slope and any surface imperfections may have allowed for a minor and premature rocking motion of the wall while the load was applied. As the rocking toe would re-contact the surface of the foundation, stiffness would continue to increase until global rocking occurred.

- Sliding of the actuator connection. The actuator connected consisted of four, hand-tightened threaded rods. For this connection to have no internal movement, both the loading beam and actuator head would have to be perfectly aligned, while the laboratory technician installed the threaded rods and hand tightened the nuts from a ladder. As a result of human error, any gaps in this connection would cause a brief instance of low stiffness as the actuator head would slide along

the threaded rods before making contact with the bearing plate on the loading beam.

- Sliding of the loading beam. Similarly to the actuator connection, the loading beam was camped to the wall by hand with threaded rods. As both the loading beam and wall had to have the connection holes pre-drilled for installation, minor offsets could allow for sliding of the loading beam along the top of the wall.

When the loading beam and actuator were reconnected for the Wall 1 test, better bolt tightening procedures were used in order to avoid any potential for sliding.

Shown in Figure 5.16 and Figure 5.17 are the complete overturning moment versus drift plots.

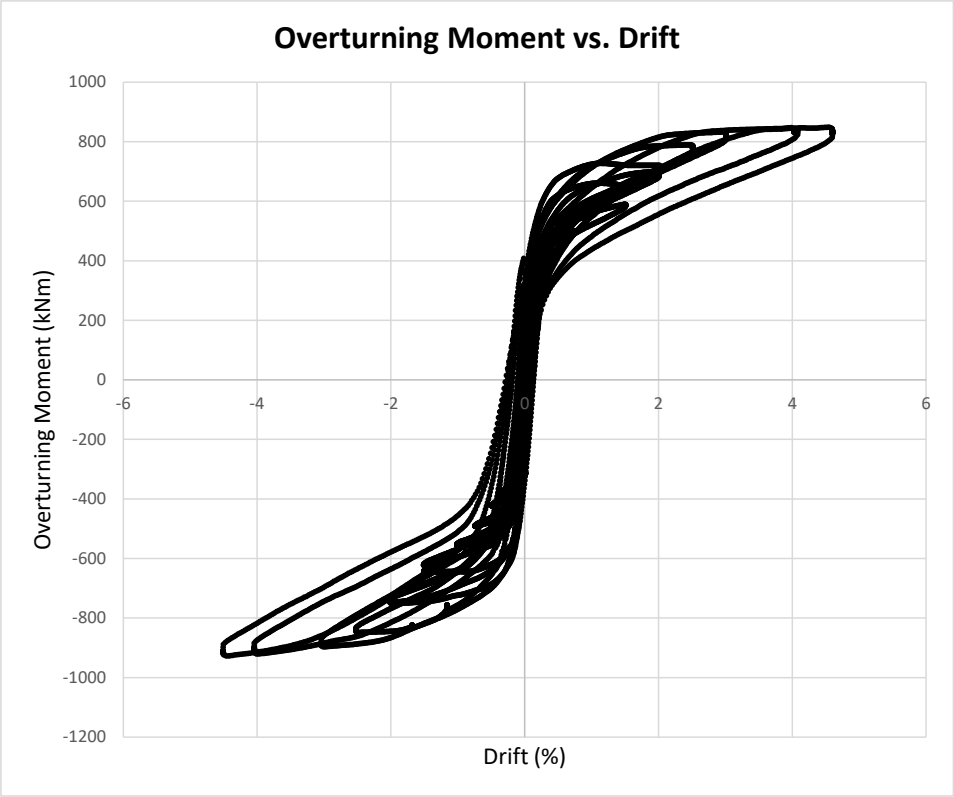

Figure 5.16: Overturning Moment vs. Drift for Wall 1

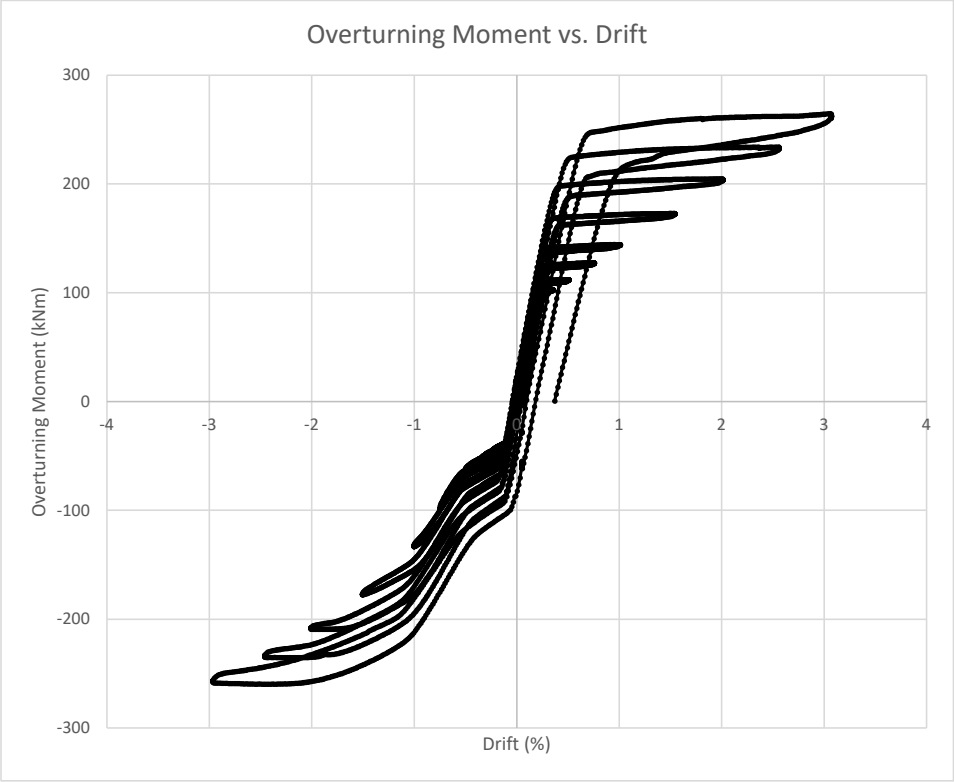

Figure 5.17: Overturning Moment vs. Drift for Wall 2

As shown in Figure 2.4, and discussed by [Newcombe, 2011] and [Marriott, 2009], the overturning moment versus drift plot at each drift depicts the expected 'flag-shape' hysteresis of a rocking system. Although there are no energy dissipation devices present in the system, there is still some small amount of inherent energy dissipation due to nonlinear response of the CLT wall. However, it is clear that the total energy dissipation is far less than when comparing to previous tests conducted by others with energy dissipation devices. This inherent energy dissipation can prove to be beneficial in structures that may require a lateral force resisting system, but are not expected to experience large seismic demands.

Shown in Figure 5.18 and Figure 5.19 are the positive motion cycles for Wall 1 and Wall 2, respectively. These figures highlight the distinctive rocking behaviour for each wall, with Wall 2 displaying more discrete rocking points as opposed to the gradual stiffness reduction shown for Wall 1. Although the axial stress for both systems remained constant, this behaviour is likely a result of

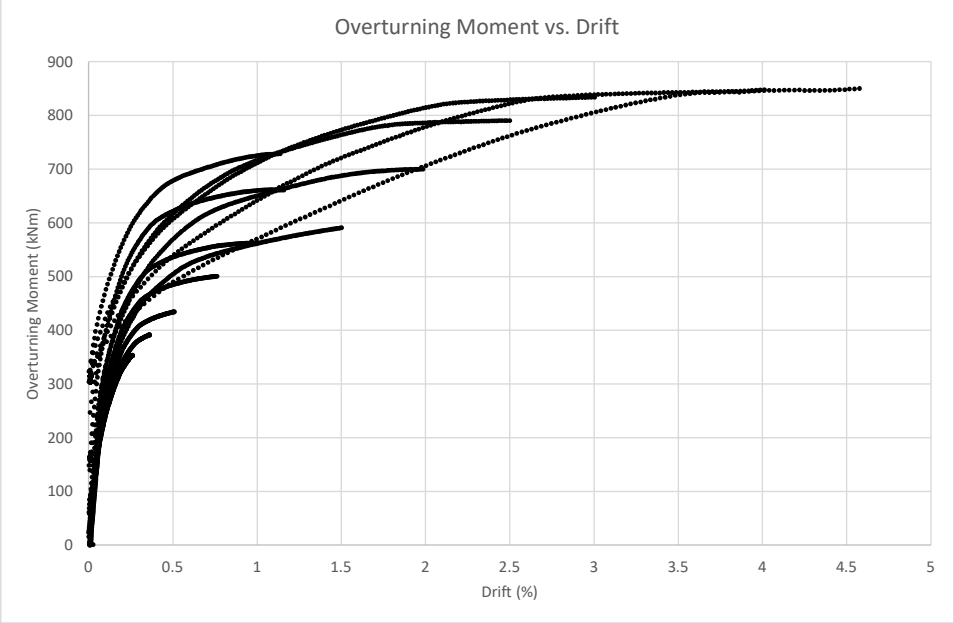

Figure 5.18: Overturning Moment vs. Drift Positive Cycles for Wall 1

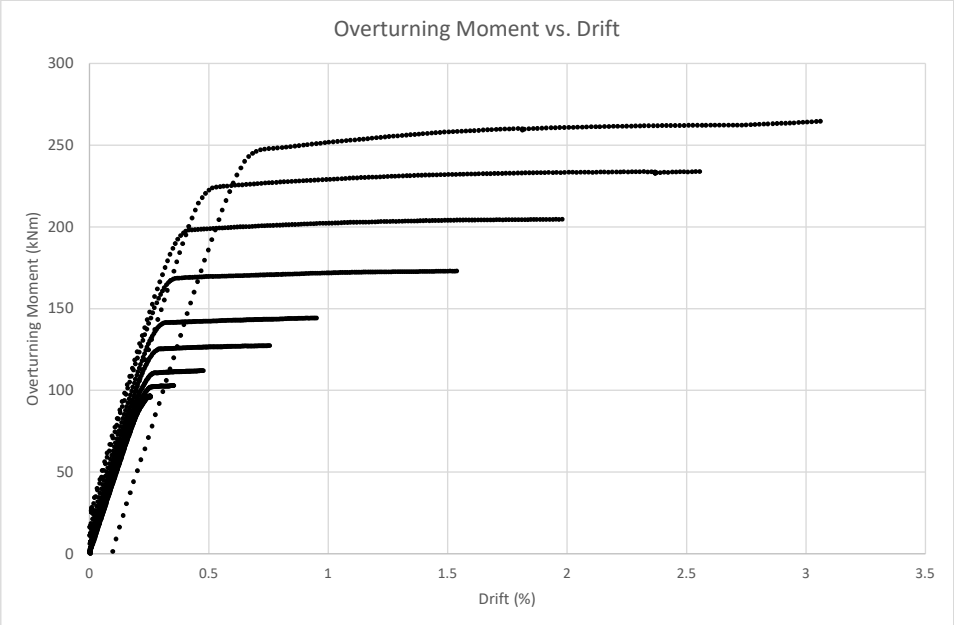

Figure 5.19: Overturning Moment vs. Drift Positive Cycles for Wall 2

the overall larger loading experienced by Wall 1, and the associated more extensive damage to the rocking toes.

5.2.3 Roof Drift and Base Rotation

The data measured by the rotary variable differential transformer (RVDT), centrally mounted at the base of the wall, is shown in Figure 5.20 and Figure 5.21, for wall 1 and wall 2, respectively. For wall 2, there were technical errors with the data collection from the RVDT for the first few cycles, so there was no data collected at low amplitudes. From Figure 5.20, the base rotation for wall 1 accounts for approximately 90% of the total drift, with the remainder coming from elastic deflection along the height of the wall. Similarly, the positive drift cycles for wall 2 exhibit the same behaviour, with approximately 90% of the total drift coming from the base rotation. As previously discussed in Section 5.2.2 with correlation to the intermediate decrease in stiffness, the negative cycles depict more elastic deformation, with approximately 80% of the drift coming from the base rotation.

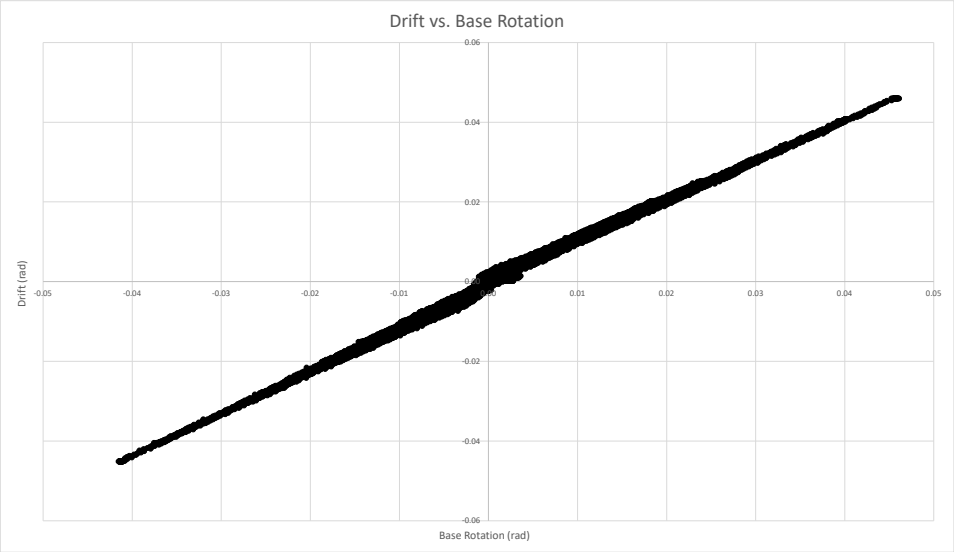

Figure 5.20: Drift vs. Base Rotation for Wall 1

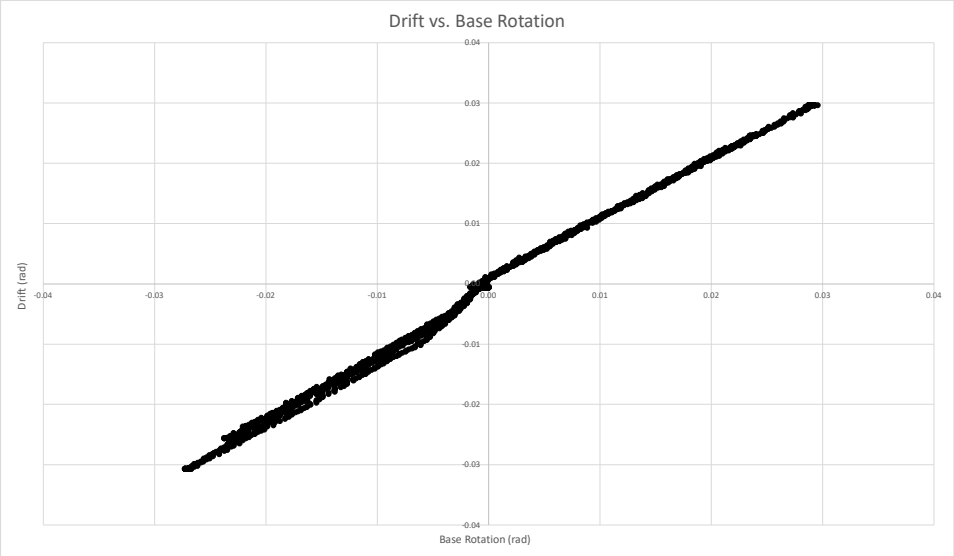

Figure 5.21: Drift vs. Base Rotation for Wall 2

5.2.4 Stiffness

Although the prediction model only requires initial stiffness as an input, a rocking CLT wall has three stiffness regions, as depicted by [Ganey, 2015] in Figure 5.22. The three regions are the initial stiffness, k_0, the decompression stiffness, k_{dec}, and the recentering stiffness, k_{rec}. As shown in Figure 5.22, the initial stiffness is defined as the stiffness prior to uplift, or decompression. The decompression stiffness is defined as the stiffness after uplift, while the wall is approaching maximum drift. Lastly, the recompression stiffness is defined as the stiffness while the wall is returning to zero drift, yet still uplifted [Ganey, 2015]. The average of these two stiffness values is the secondary stiffness.

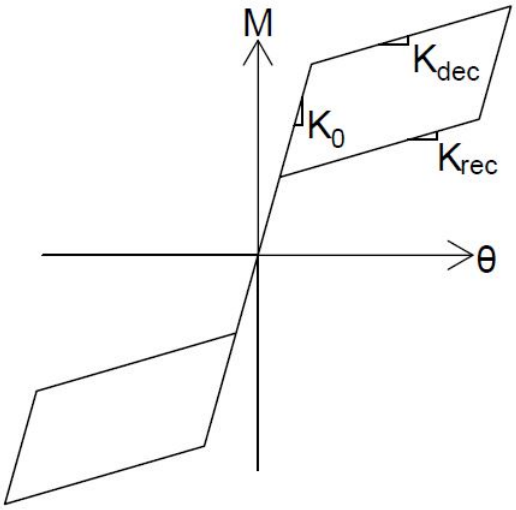

Figure 5.22: Idealized Flag Shaped Hysteresis Showing System Stiffness [Ganey, 2015]

For each hysteretic loop, the three stiffness stages were identified manually and a linear regression analysis was performed on each stage. The slope of the linear regression is the experimental stiffness value. The system stiffness values were taken as the average from each cycle. The cyclic and average values are shown in Table 5.1 for wall 1, and Table 5.2 for wall 2.

Table 5.1: System Stiffness Values - Wall 1

Cycle *Drift %*	Average Initial Stiffness	Average Secondary Stiffness	Decompression Stiffness k_{dec}	Recentering Stiffness k_{rec}
0.25	11.850	3.154	3.056	3.253
-0.25	12.587	1.327	1.174	1.480
0.35	12.822	1.389	1.326	1.452
-0.35	11.304	0.749	0.628	0.869
0.50	13.581	0.509	0.466	0.552
-0.50	11.262	0.491	0.556	0.427
0.75	15.113	0.288	0.290	0.286
-0.75	14.861	0.445	0.485	0.406
1.00	14.548	0.277	0.251	0.303
-1.00	12.387	0.312	0.234	0.389
1.50	10.417	0.358	0.273	0.443
-1.50	8.349	0.327	0.289	0.365
2.00	9.610	0.355	0.304	0.406
-2.00	7.841	0.348	0.322	0.375
2.50	8.384	0.372	0.340	0.404
-2.50	7.273	0.454	0.446	0.461
3.00	7.001	0.458	0.445	0.470
-3.00	6.270	0.558	0.534	0.583
4.00	5.926	0.361	0.351	0.372
-4.00	5.322	0.464	0.534	0.464
System Average:	10.335	0.649	0.615	0.688

Table 5.2: System Stiffness Values - Wall 2

Cycle *Drift %*	Average Initial Stiffness	Average Secondary Stiffness	Decompression Stiffness k_{dec}	Recentering Stiffness k_{rec}
0.25	1.593	0.190	0.159	0.220
-0.25	1.779	0.780	0.780	0.780
0.35	1.639	0.182	0.176	0.188
-0.35	1.772	0.043	0.028	0.057
0.50	1.626	0.191	0.183	0.198
-0.50	1.828	0.037	0.029	0.046
0.75	1.794	0.237	0.274	0.200
-0.75	1.855	0.022	0.016	0.028
1.00	1.817	0.362	0.308	0.416
-1.00	1.879	0.024	0.019	0.029
1.50	1.839	0.407	0.200	0.615
-1.50	1.890	0.022	0.018	0.026
2.00	2.296	0.189	0.178	0.200
-2.00	1.943	0.024	0.017	0.031
2.50	2.205	0.063	0.123	0.004
-2.50	1.873	0.032	0.020	0.040
3.00	1.472	0.081	0.107	0.055
-3.00	1.465	0.102	0.135	0.070
System Average:	1.809	0.166	0.154	0.178

A comparison of the initial stiffnesses and secondary stiffnesses for both the positive and negative drift ranges are given in Figures 5.23 and 5.24. Generally, the initial stiffness values decreased as the test continued, with the first positive cycle showing a larger stiffness value than the following negative cycle, which is to be expected. With regards to the secondary stiffnesses for wall 1, after the first few cycles, both the positive and negative cycles show similar values while also remaining relatively constant as the test progressed. This consistency in secondary stiffness can also be seen when separating the average secondary stiffness into its decompression and recentering stiffness components, shown in Figure 5.25. Generally similar stiffness behaviour was also exhibited in wall 2, shown in Figures 5.26-5.28, except that the secondary stiffness does not behave in the same manner as wall 1. For wall 2, the secondary stiffness values do not match for the positive and negative cycles, as shown in Figure 5.27. This difference is a direct result of the analysis method for each hysteretic cycle, previously explained. Since wall 1 depicted the ideal flag-shaped hysteresis, the linear regression and best fit method produce accurate and similar results for both the positive and negative cycles. However, due to the irregularity of wall 2's hysteretic behaviour, this method did not produce results that closely aligned. Shown in Figure 5.29 are the results of the stiffness analysis for each cycle up to 1.5% drift for wall 2, demonstrating the challenge of describing the rocking behaviour with a single secondary stiffness.

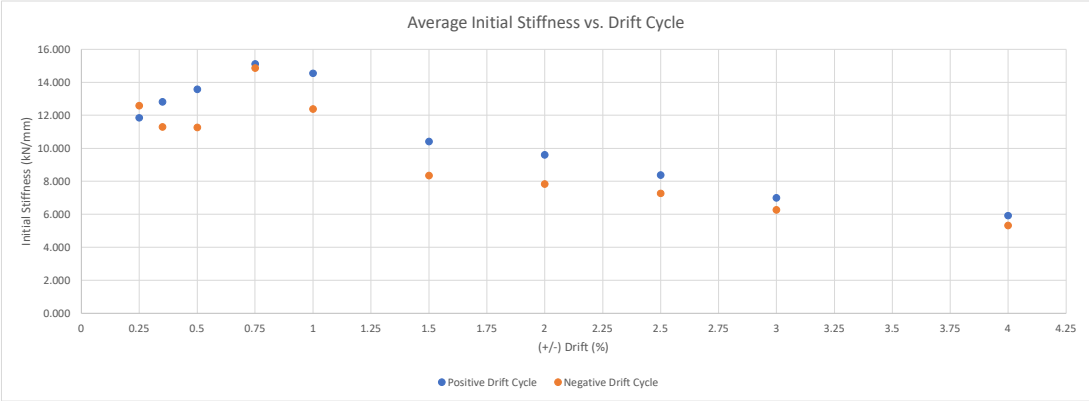

Figure 5.23: Average Initial Stiffness Values for Positive and Negative Drift Cycles - Wall 1

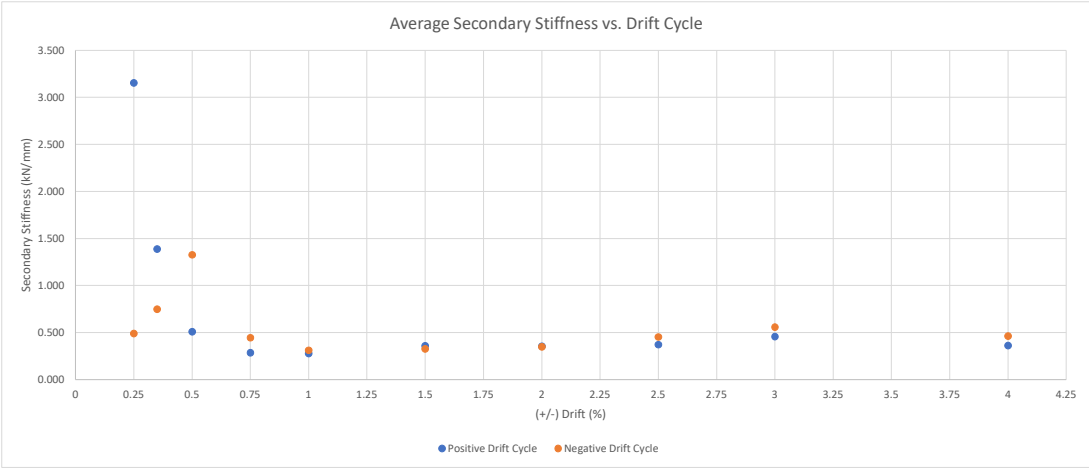

Figure 5.24: Average Secondary Stiffness Values for Positive and Negative Drift Cycles - Wall 1

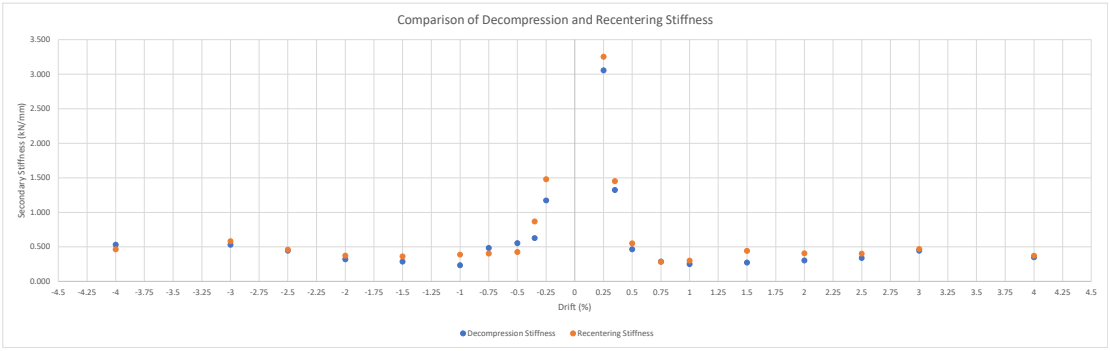

Figure 5.25: Comparison of Decompression and Recentering Stiffness - Wall 1

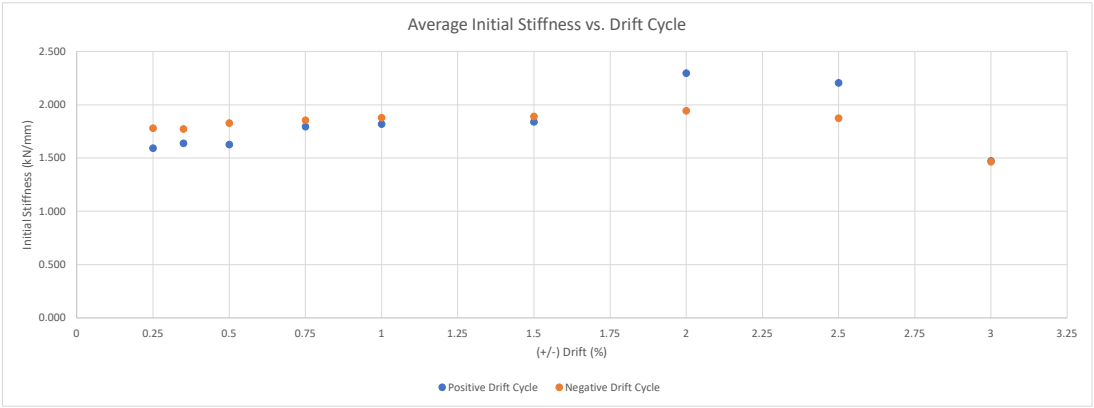

Figure 5.26: Average Initial Stiffness Values for Positive and Negative Drift Cycles - Wall 2

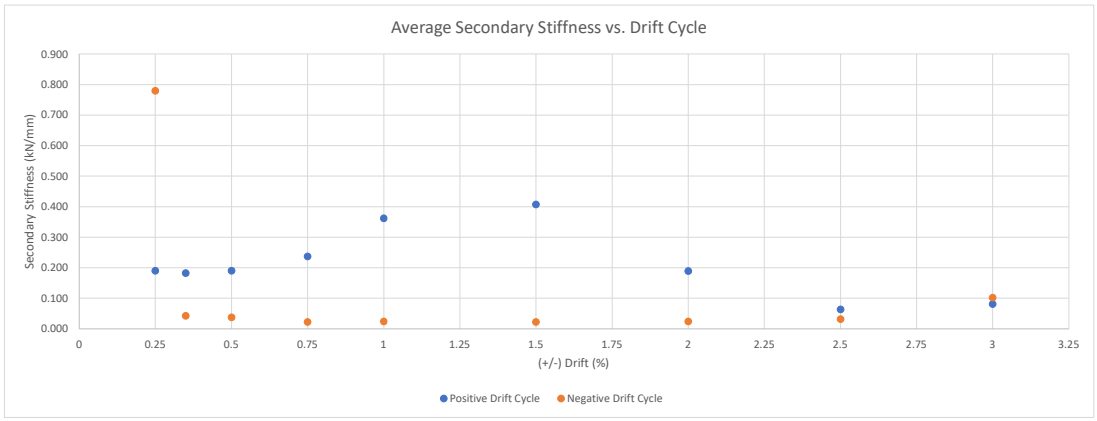

Figure 5.27: Average Secondary Stiffness Values for Positive and Negative Drift Cycles - Wall 2

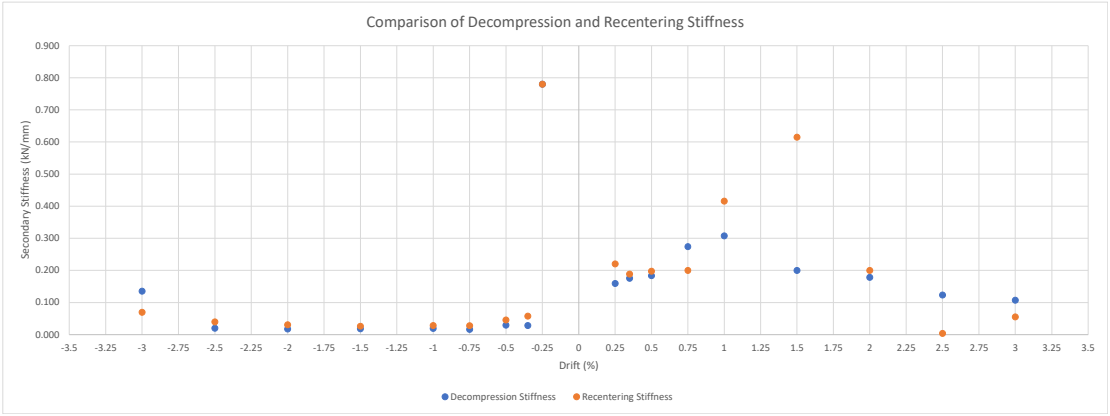

Figure 5.28: Comparison of Decompression and Recentering Stiffness - Wall 2

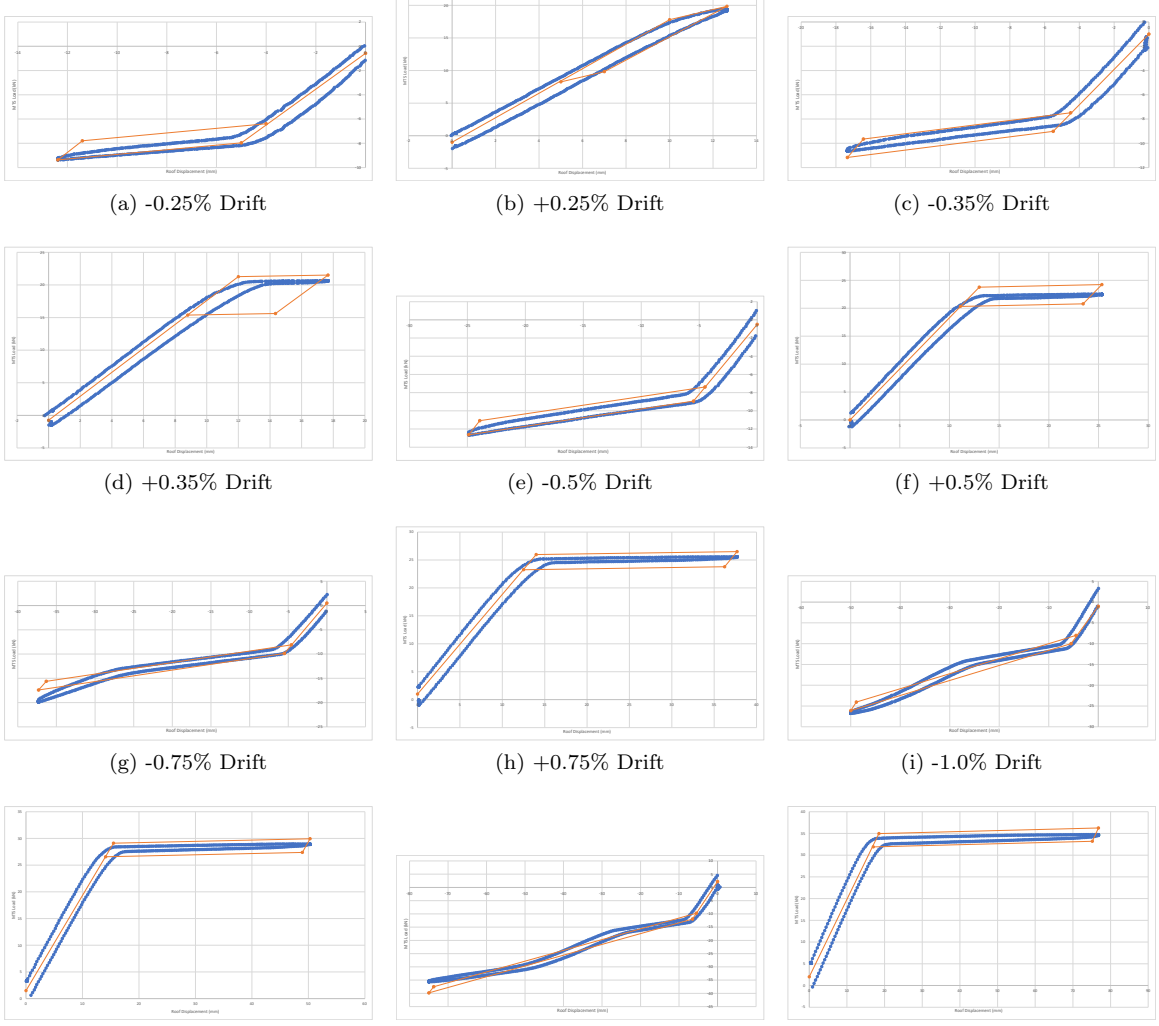

(a) -0.25% Drift (b) +0.25% Drift (c) -0.35% Drift

(d) +0.35% Drift (e) -0.5% Drift (f) +0.5% Drift

(g) -0.75% Drift (h) +0.75% Drift (i) -1.0% Drift

(j) +1.0% Drift (k) -1.5% Drift (l) +1.5% Drift

Figure 5.29: Stiffness Analysis for Wall 2 - Test Data shown in Blue

5.2.5 Energy Dissipation

The energy dissipated was calculated as the summation of the area under the force versus displacement plot. Since the axial force tendons were rated at a much higher load capacity than what they experienced, it can be assumed that the energy dissipation came strictly from the CLT panel. As can be seen in Figure 5.16 and Figure 5.17, each loading cycle dissipated more energy than the previous. The energy dissipated per cycle for Wall 1 and Wall 2 are shown in Table 5.3 and Table 5.4, respectively.

Table 5.3: Energy Dissipation per Loading Cycle for Wall 1

Cycle (% drift)	Energy Dissipation Per Cycle (J)
-0.25	82
0.35	57
-0.35	108
0.50	78
-0.50	149
0.75	138
-0.75	244
1.00	246
-1.00	415
1.50	563
-1.50	1850
2.00	1889
-2.00	3188
2.50	3719
-2.50	3365
3.00	4149
-3.00	4285
4.00	5628
-4.00	5820
4.00	7315
Total:	39131

Table 5.4: Energy Dissipation per Loading Cycle for Wall 2

Cycle (% drift)	Energy Dissipation Per Cycle (J)
0.25	11
-0.25	26
0.35	17
-0.35	33
0.50	30
-0.50	42
0.75	56
-0.75	64
1.00	90
-1.00	88
1.50	158
-1.50	177
2.00	271
-2.00	359
2.50	422
-2.50	819
3.00	624
-3.00	1287
Total:	4583.25

By analyzing the hysteresis loop for each loading cycle,as discussed in Section 5.2.4 to determine experimental stiffness, individual beta values were determined for each loading phase. For example, consider the 2.5% load cycle, shown in Figure 5.30. The primary and secondary stiffness values were determined through a linear regression analysis. Using the total energy dissipated, the rocking load, and the peak drift, beta was determined as follows:

$$\beta = \frac{4138.5J}{[(-125.6mm) - (-20mm)](-137.4kN)} = 0.285 \tag{45}$$

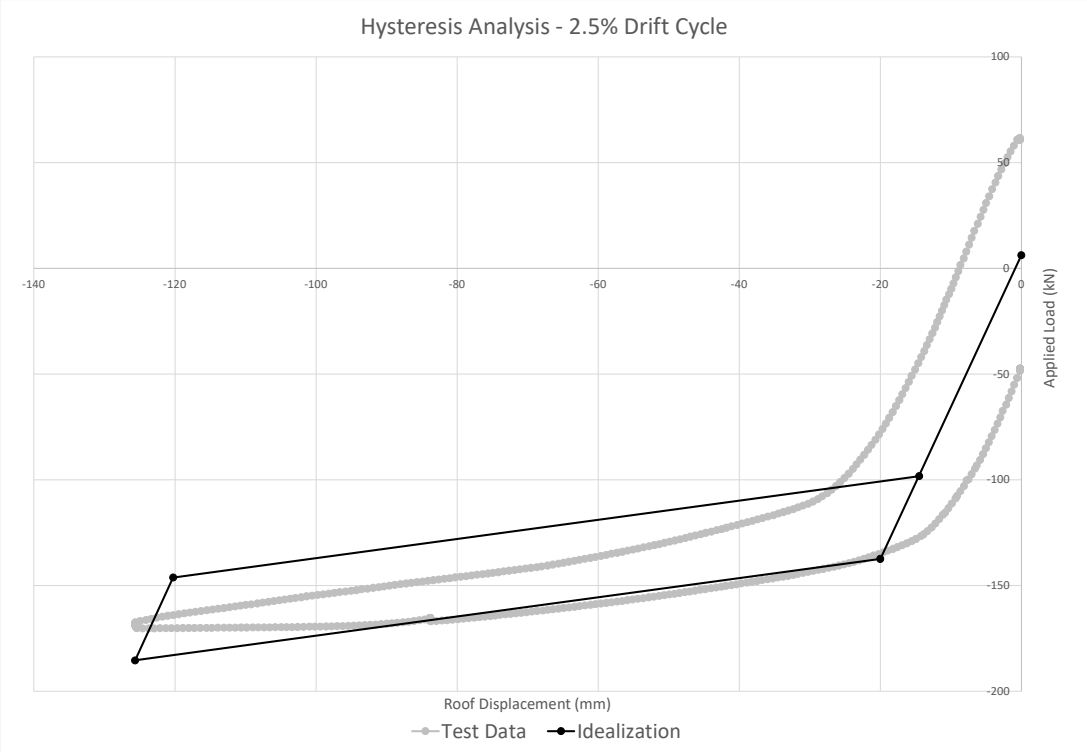

Figure 5.30: 2.5% Loading Cycle Analysis Example

The beta values per cycle are shown in Figure 5.31. To obtain the system beta value, each individual value was multiplied by a weight factor determined by dividing the energy dissipated per cycle by the total energy dissipation. These values were then summed to obtain the system beta value of 0.265 for wall 1, and 0.161 for wall 2.

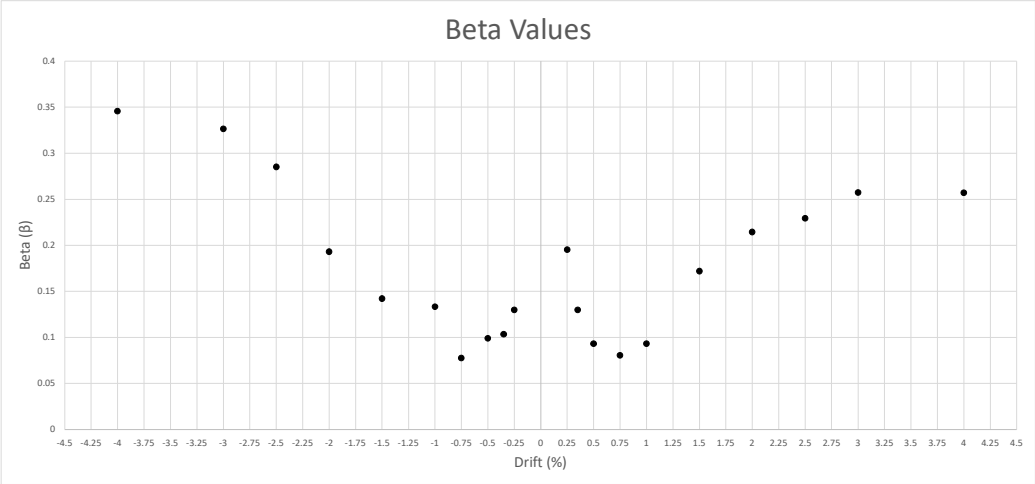

(a) Beta Values per Loading Cycle for Wall 1

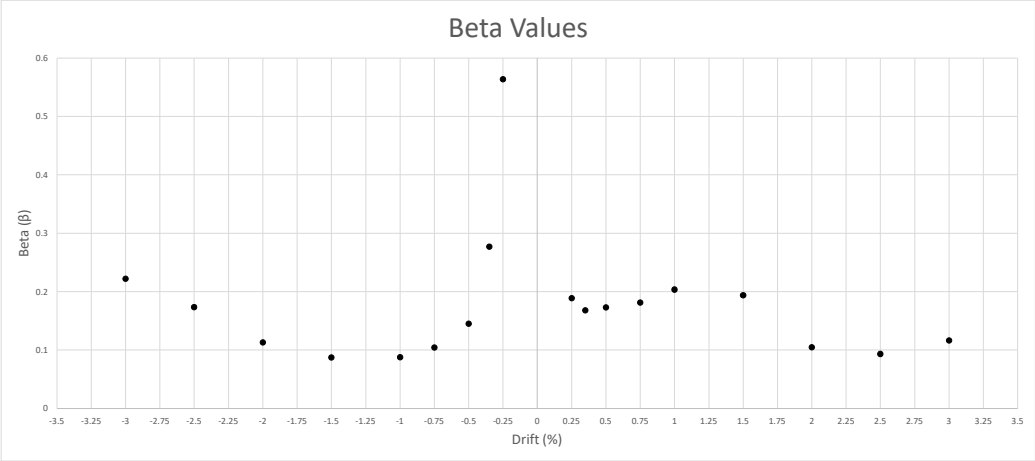

(b) Beta Values per Loading Cycle for Wall 2

Figure 5.31: Beta Values for Each Loading Cycle

5.2.6 Residual Drift

The residual drift of the system at each phase of the experiment was taken as the lateral displacement reading at zero lateral force. Figure 5.32 and Figure 5.33 show the residual drifts for each loading cycle. Upon completion of the test, the residual drift of the system was 13 mm (0.25%) and 1.6 mm (0.03%), for wall 1 and wall 2 respectively. Wall 1 slightly exceeded the prescribed limit of 0.2%, outlined in [ATC, 2012].

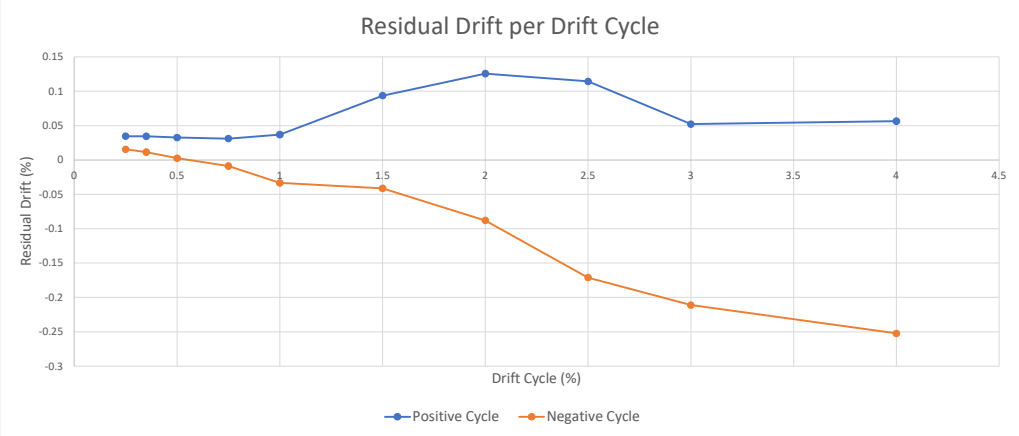

Figure 5.32: Residual Drift per Drift Cycle - Wall 1

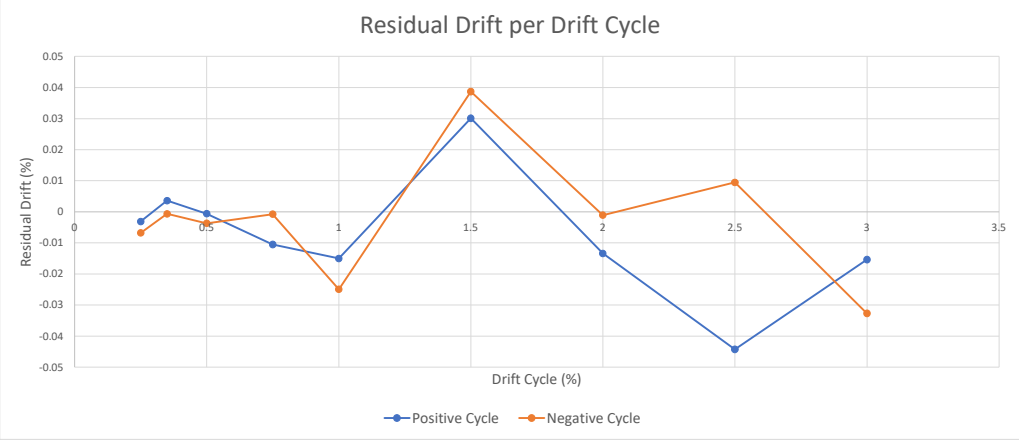

Figure 5.33: Residual Drift per Drift Cycle - Wall 2

5.2.7 Base Profile and Neutral Axis Depth

As discussed in Section 2.5.1, the neutral axis depth is the length of wall that is in compression, or in contact with the with the ground. As the wall begins to decompress, the neutral axis approaches the rocking toe. In addition to the neutral axis depth, the base profile also includes the uplift of the toe that is not in compression. The uplift along the length of the wall base was determined using six equally spaced string potentiometers, as discussed in Section 4.3. The neutral axis depth was approximated through linear interpolation between the two potentiometers reading a positive value at one point, and a negative value at the next.

Shown in Figure 5.34 are the string potentiometer profiles for wall 1 and 2 at different levels of drift. At the maximum achieved drift, an uplift of 73mm and 32mm was measured for wall 1 and wall 2 respectively. As discussed in Section 5.1, noticeable uplift had not occurred until after a few cycles, even though the neutral axis depth rapidly decreased during the first loading cycles. From Figure 5.34a and 5.34b, this rapid decrease of the neutral axis depth is clear as string potentiometers 2 to 6 all show decompression. Therefore, even though noticeable uplift may not have occurred, the majority of the wall base had decompressed.

Figure 5.35 and Figure 5.36 show the percentage of the wall that is in compression for each level of drift for wall 1 and wall 2, respectively. Similar to the findings of [Ganey, 2015], the neutral axis depth rapidly decreased as the wall decompressed and then steadied out around 20% of the base length. However, as more damage occurs at the base of the wall, a larger portion of the wall would be under compression, as can be seen in Figure 5.36 for wall 2.

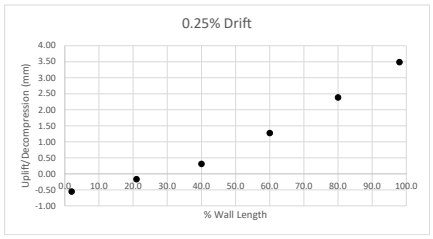

(a) Wall 1 0.25% Drift

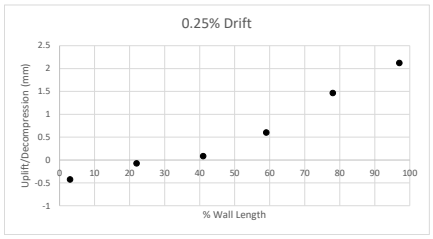

(b) Wall 2 0.25% Drift

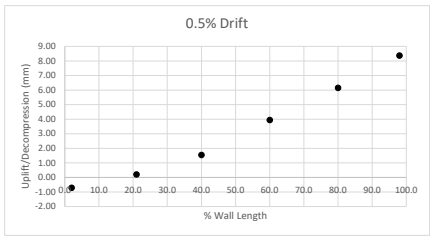

(c) Wall 1 0.50% Drift

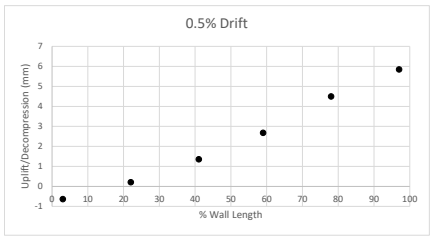

(d) Wall 2 0.50% Drift

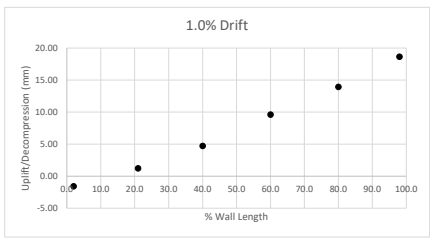

(e) Wall 1 1.0% Drift

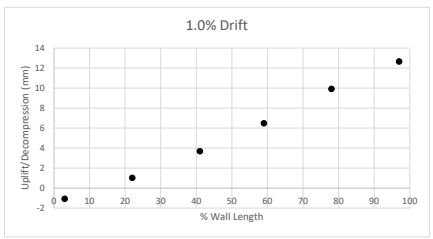

(f) Wall 2 1.0% Drift

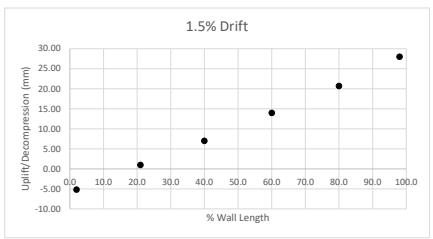

(g) Wall 1 1.5% Drift

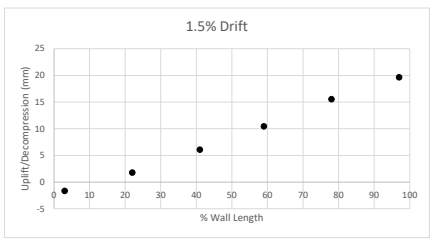

(h) Wall 2 1.5% Drift

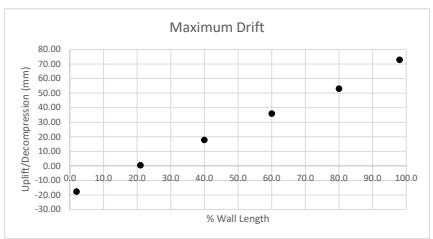

(i) Wall 1 Maximum Drift 4.5%

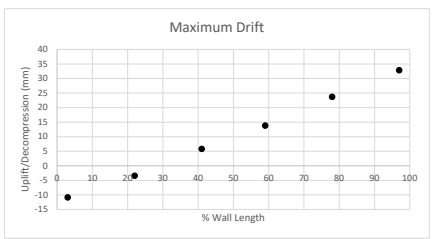

(j) Wall 2 Maximum Drift 3.0%

Figure 5.34: Comparison of String Potentiometer Profiles at Different Levels of Drift

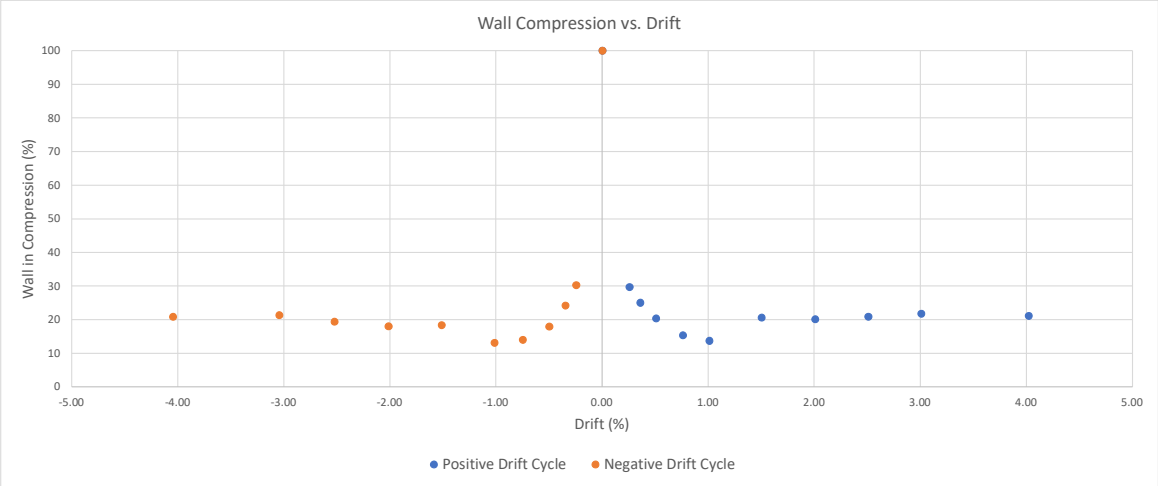

Figure 5.35: Neutral Axis Depth (%) per Drift Cycle - Wall 1

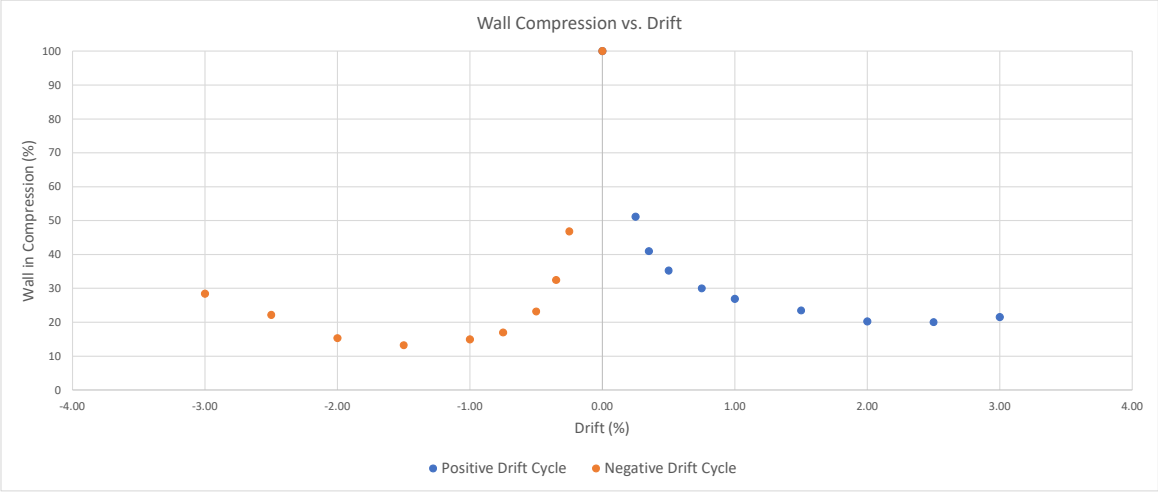

Figure 5.36: Neutral Axis Depth (%) per Drift Cycle - Wall 2

5.2.8 Strains up the Wall Height

Shown in Figure 5.37 and Figure 5.38 are the strain gauge readings up the height of the wall for wall 1 and wall 2, respectively. It was expected that the gauges closer to the base of the wall would read higher strains with residuals should damage occur. This behaviour was demonstrated on the west side gauges for wall 1, shown in Figure 5.38a. However, the remaining strain gauge data did not display these expected results, nor was there any behavioural trend. This may be the result of a more complex strain field within the CLT than originally assumed, requiring an update to the prediction model. However, the readings may also not be reliable because of the limitations of strain gauges on wood. It is recommended that this, and future data collected via strain gauges on CLT, be confirmed through the use of DIC or similar.

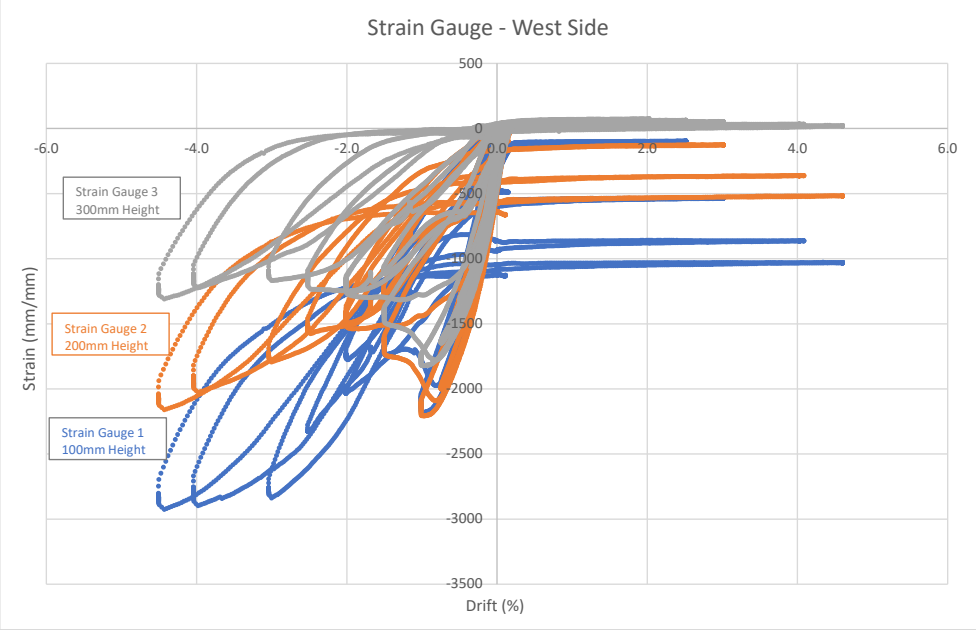

(a) Strain Gauge Data - Wall 1 West Side

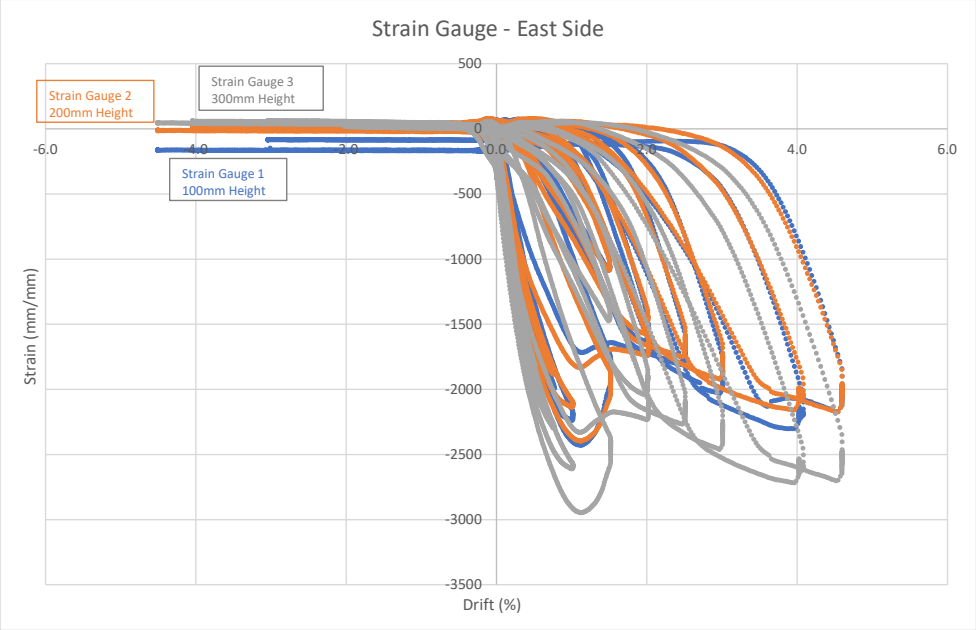

(b) Strain Gauge Data - Wall 1 East Side

Figure 5.37: Strain Gauge Data up the Height of Wall 1

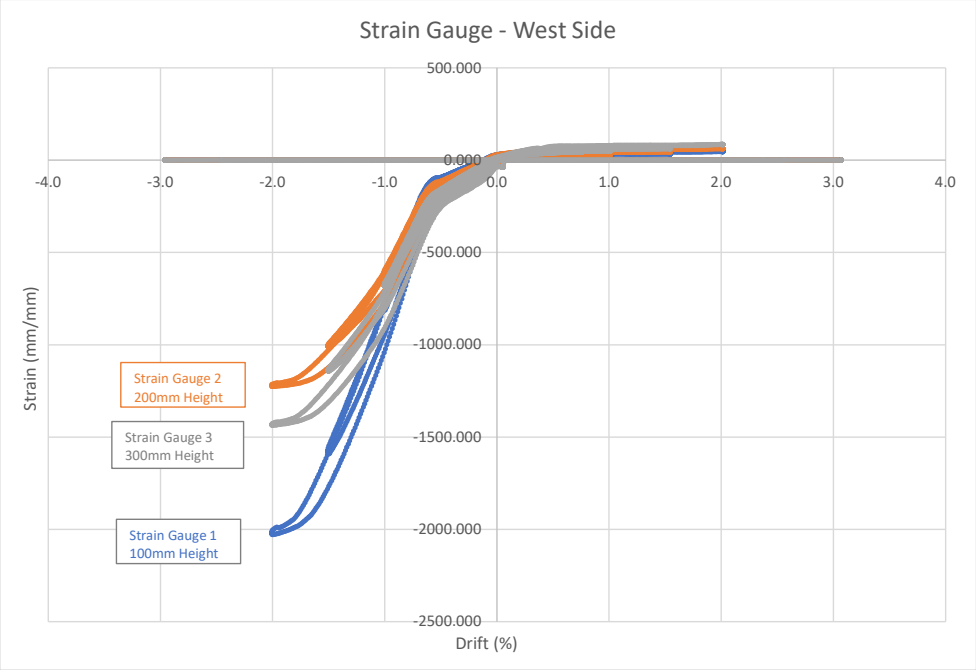

(a) Strain Gauge Data - Wall 2 West Side

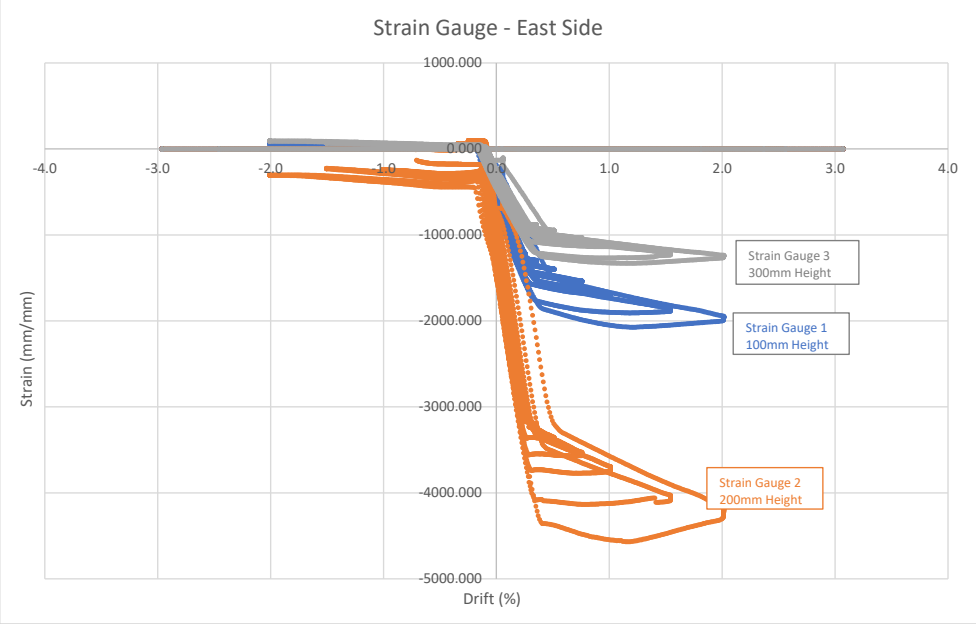

(b) Strain Gauge Data - Wall 2 East Side

Figure 5.38: Strain Gauge Data up the Height of Wall 2

6 Comparison to Prediction Model

This section compares the prediction models presented in Section 2.5 with the experimental results in Section 5. The prediction is then updated with data from the experimental procedure to further analyze the accuracy of the model.

6.1 Preliminary Prediction Model

When comparing the preliminary prediction model, which utilized the Winkler Spring approximation with expected CLT properties, to the experimental results for Wall 1, the prediction model underestimates the overturning moment at lower drifts, while overestimating at large drifts, shown in Figure 6.1. With regards to Wall 2, the prediction model consistently underestimates the overturning moment, which can be seen in Figure 6.2.

In comparison to the experimental maximum plots, shown for Wall 1 in Figure 6.1, the Winkler Spring model underestimates the experimental results by approximately 20% between 0 and 3% drift, while overestimating the overturning moment by 10% at 4% drift. Similar to the underestimation of Wall 1, the Winkler Spring model underestimates the experimental maximum values of Wall 2 by 20%-30%, decreasing with larger drift ranges, as shown in Figure 6.2.

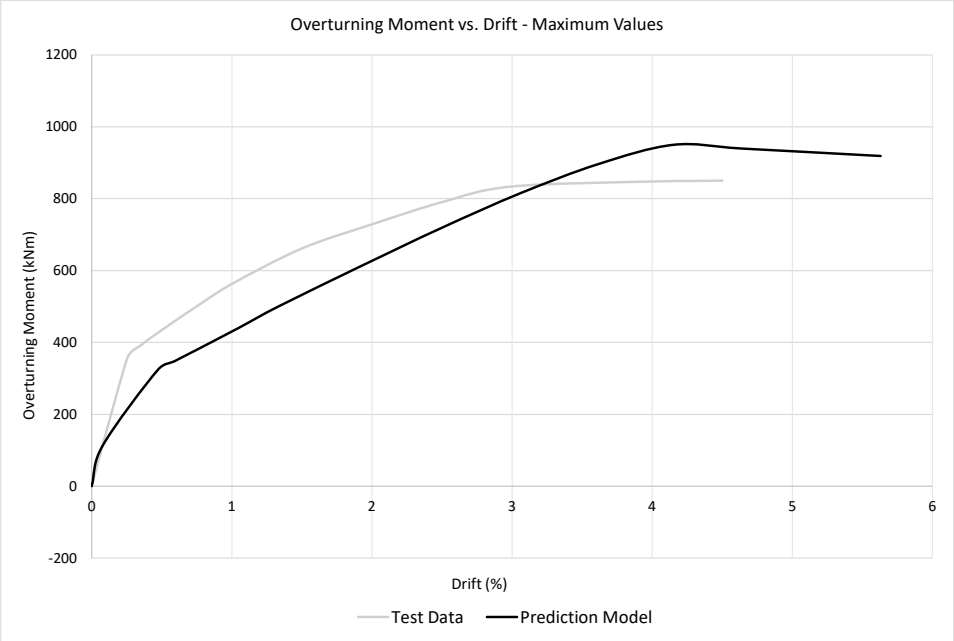

Figure 6.1: OTM vs. Drift - Comparison with Original Winkler Approximation - Wall 1

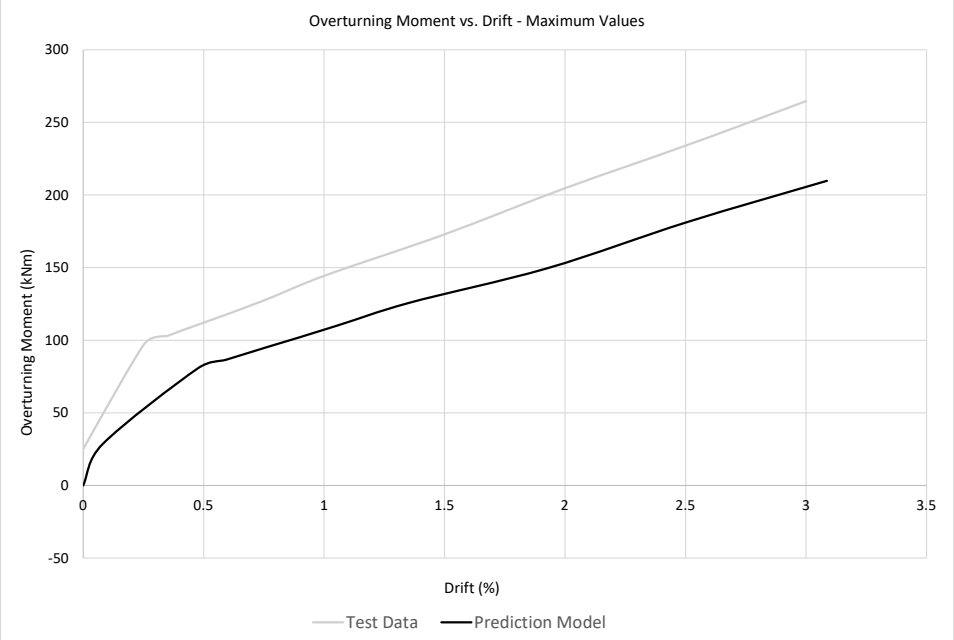

Figure 6.2: OTM - Comparison with Original Winkler Approximation - Wall 2

6.2 Updated Prediction Model

At the conclusion of the test, the prediction model was re-calibrated using the data collected during the experimental procedure. The initial stiffness was updated using the values determined in Section 5.2.4, while the post-tensioning values were updated using those measured by the MTS system, though the post-tensioning values did not differ by much. In comparison to the value used in the preliminary model, the initial stiffness was greatly underestimated by approximately 50% for Wall 1. For Wall 2, the value was only underestimated by approximately 20%.

As discussed in Section 2.5, the simplicity of these models only calls for the use of the initial stiffness. Using the test results shown in Table 5.1 and Table 5.2, the initial stiffness values for both walls were updated, and thus the updated prediction model results are provided in Figure 6.3 and Figure 6.4. The updated Winkler Spring model approximates both Walls to within 10% accuracy of the experimental results, as compared to the original 20% at lower drifts and the overestimation at higher drifts. In addition, the use of the real axial load allowed for improvement of the peak estimate. Although the updated model is a much closer approximation, Wall 2 is still consistently underestimated. This underestimation is likely due to an error in stiffness estimation method used. Although the same process was used for Wall 1, the analysis for Wall 2 was more difficult due to the smaller loads involved.

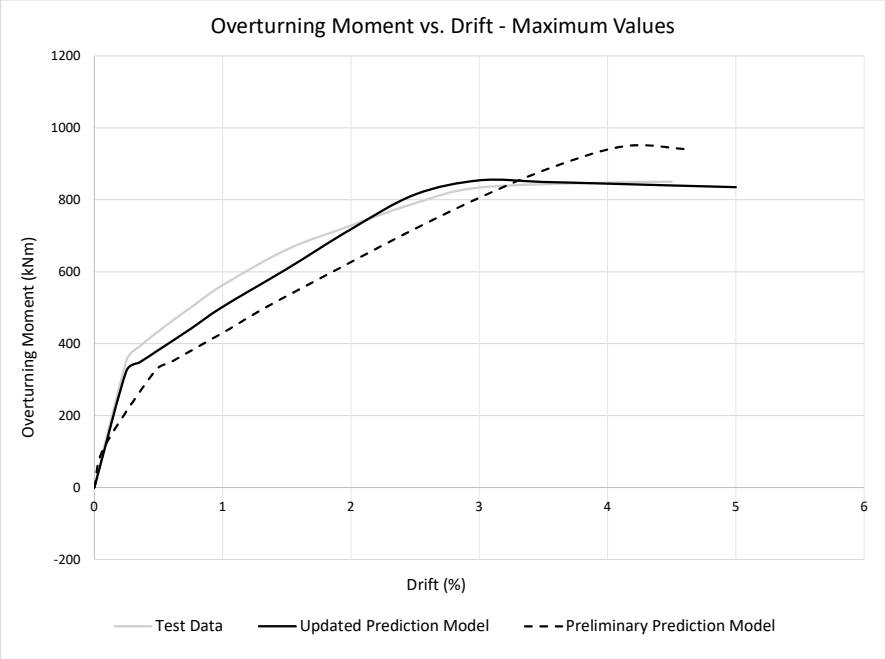

Figure 6.3: OTM - Comparison with Updated Winkler Approximation - Wall 1

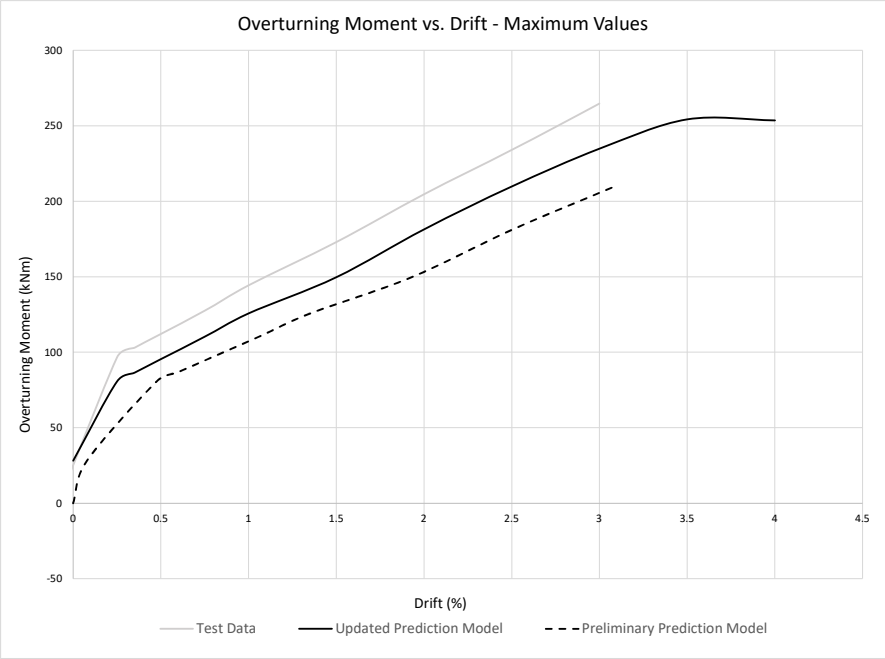

Figure 6.4: OTM - Comparison with Updated Winkler Approximation - Wall 2

7 Conclusions and Recommendations for Future Research

This chapter reviews the findings and conclusions developed during this study, and recommends areas of potential future research.

7.1 Summary and Conclusions

This purpose of this thesis was to gain a better understanding of the behaviour of CLT walls when used in a controlled rocking system. The most critical area of analysis in this study was the rocking toe. Using previously developed prediction models, the behaviour of the rocking toe was predicted, and later analyzed and evaluated through large-scale experimental procedures.

Simplified methods of analysis for rocking CLT systems have been introduced by others, including the Monolithic Beam Analogy [Pampanin et al., 2001], and later the Winkler Spring model. In this study, two large-scale CLT walls were designed, utilizing the Winkler Spring model, as well as the findings from Kovacs and Wiebe (2016), Sarti (2015), Ganey (2015), and Newcombe (2005-2015). The two CLT walls differed in width and thickness, and were subjected to a to quasi-static reverse cyclic loading protocol.

As originally presented by Newcombe (2011), and later confirmed by Kovacs and Wiebe (2016), the Winkler Spring analogy was employed in this study as it has the capability of accurately predicting the behaviour of the rocking toe in a rocking CLT application. A prototype structure was designed following current force-based design procedures of the NBCC, with an overall drift limit of 2.5%. Half-scale CLT panels were subjected to a quasi-static reverse cyclic loading protocol, and the results were compared with the prediction models utilizing the Winkler Spring analogy.

Both walls had depicted the expected 'flag-shaped' hysteresis, and even without the use of energy dissipation devices, there was still a significant amount of inherent energy dissipation due to the nonlinear response of the CLT walls (average beta of 0.265 and 0.161 for Walls 1 and 2, respectively). Although Wall 2 had a region of unexpected hysteretic response, where a slight decrease in stiffness occurred, it was concluded that this was likely due to the uneven rocking interface during this test and/or sliding of the bolted connection. Through the use of a centrally mounted RVDT, it was shown that the majority of the roof drift, 80%-90%, came from base rotation, with the remainder coming

from elastic deflection. Upon completion of the tests, the residual drift of the system was 13mm (0.25%) for Wall 1 and 1.6mm (0.03%) for Wall 2. Estimation methods were utilized to determine the system stiffness values for each wall. This estimation method was challenging to complete for Wall 2 and may have resulted in somewhat erroneous values. However, for the majority of the stiffness data, similar trends were followed in both loading directions. Within the toe region, multiple strain gauges were applied up the height of the wall. The data collected did not depict the expected result, implying that a complex strain field exists within the toe region of the CLT.

The preliminary prediction model, which utilizes material test values, was able to predict the rocking behviour of the the CLT panels to within 30% of the measured experimental values. These models were then updated after the experimental procedure with data gathered during the large-scale tests. The updated model brought the predictions to within 10% accuracy for both walls; however, the model consistently underestimates the lateral resistance both at lower levels of drift and for the panel with the smaller aspect ratio. This underestimation, specifically with regards to Wall 2, is likely due to the error in the stiffness estimation methods used. Although the model is close, there is still room from improvement.

7.2 Recommended Future Research

Further Calibration of Winkler Spring Analogy

Newcombe (2011) proposed the Winkler Spring Analogy as a solution to his concerns with the Monolithic Beam Analogy, summarized in Section 2.5.2. This new proposed method included a relationship between the wall length and neutral axis depth, known as the Winkler Spring effective length. This new value would essentially account for the reduced axial stiffness, in comparison to the MBA. Although his studies found his proposed empirical equation was accurate, Newcombe's tests were performed on LVL panels. Furthermore, design approaches differ depending on geographical location. For this study, Newcombe's proposed Winkler Spring effective length was utilized and the prediction models were able to accurately predict the CLT behaviour to within 10% accuracy. It is recommended that further research be conducted on the modification of this relationship in order to increase prediction accuracy. In addition, these modifications may require further iteration as CLT manufacturing in Canada, with Canadian timber species, continues to develop.

Canadian CLT and Fabrication Methods

As CLT production and use for lateral load resisting system is relatively new, many manufacturers are still developing and perfecting their fabrication methods. As they continue to develop, better and more reliable production will be achieved. For this study, the manufacturer had not yet established full confidence in in the material property values they provided. Upon completion of the material tests, it was clear that the given values drastically varied from those gathered experimentally. In addition to, and also related to, the material properties, the improvement in physical construction of the CLT panels will aid in achieving uniformity and reliability in the data provided by manufacturers. Shown in Section 6.2 is the updated prediction model which utilizes data gathered from both the large-scale and material tests. Should the manufacturer provided data be more accurate and reliable, increased accuracy of initial prediction models can be achieved.

Alternative Strain Measurements of the Rocking Toe

In this study, strain and displacement readings were taken at discrete points. Behavioural assumptions were made for the areas between these points. These assumptions are directly related to the Winkler Spring analogy, in defined how the theoretical springs behave. A more accurate approach would involve gathering data across the entire wall base, as opposed to at discrete points. One such method is digital image correlation, discussed in Section 4.4. Although such an analysis is not within the scope of research, digital image correlation data was gathered during the experimental procedure. It is recommended that further research be conducted in this area to help support the findings of this study, as well as aid in the development of an improved prediction model.

Coincidentally, at the time of writing, a study by [Brown et al., 2020] incorporates a similar process to DIC in his research of the rocking toe behaviour of CLT walls. Referred to as particle tracking technology (PTT) in his paper, he applies stickers to the surface of the timber and tracks the movement of the 'particles'. [Brown et al., 2020] found that this method was able to capture the complex strain fields on the timber surface, aiding in the conclusion that the behavioural assumption used in herein require further development.

Construction Applications

Although the experiments performed for this study, as well as previous studies, have been large-scale tests, further research is required to determine the most appropriate methods to incorporate

these lateral load resisting systems into real-life structures, both new and existing. These connections must allow for the proper transfer of load, while also allocating enough space and resources for these systems to be accessed, assessed, and replaced if necessary.

References

[ACI, 2007] ACI (2007). ITG-5.1-07 Acceptance Criteria for Special Un- bonded Post-Tensioned Precast Structural Walls Based on Validation Testing. Technical report.

[Amaris Mesa, 2010] Amaris Mesa, A. (2010). *Developments of Advanced Solutions for Seismic Resisting Precast Concrete Frames.* Doctor of philosophy, University of Canterbury.

[ATC, 1996] ATC (1996). ATC-40 Seismic Evaluation and Retrofit of Concrete Buildings. 1(November 1996):612.

[ATC, 2012] ATC (2012). FEMA P58 seismic performance assessment of buildings. Technical report.

[Blass and Fellmoser, 2004] Blass, H. J. and Fellmoser, P. (2004). Design of solid wood panels with cross layers. In *Proceedings of the 8th World Conference on Timber Engineering*, number 2, pages 543–548.

[Bradley and Cubrinovski, 2011] Bradley, B. A. and Cubrinovski, M. (2011). Near-source strong ground motions observed in the 22 February 2011 Christchurch earthquake. *Bulletin of the New Zealand Society for Earthquake Engineering*, 44(4):181–194.

[Bradley et al., 2009] Bradley, B. A., Dhakal, R. P., MacRae, G. A., and Cubrinovski, M. (2009). Prediction of Spatially Distributed Seismic Demands in Specific Structures: Structural Response to Loss Estimation. *Earthquake Engng. Struct. Dyn.*, 39(6):591–613.

[Brown et al., 2020] Brown, J., Li, M., Nokes, R., Palermo, A., Pampanin, S., and Sarti, F. (2020). Investigating the compressive toe of pos-tensioned CLT core-walls use Particle Tracking Technology. *17th World Conference on Earthquake Engineering, 17WCEE*, pages 1–12.

[Bruneau and MacRae, 2017] Bruneau, M. and MacRae, G. (2017). Reconstructing Christchurch : A Seismic Shift in Building Structural Systems. Technical report, Quake Centre.

[Canadian Standards Association, 2009] Canadian Standards Association (2009). *Engineering Design in Wood*. CSA O86-14, Missassauga, ON.

[Christopoulos et al., 2001] Christopoulos, C., Filiatrault, A., Uang, C., and Folz, B. (2001). Post-tensioned energy dis- sipating connections for moment-resisting steel frames. *Journal of Structural Engineering*, 128(9):1111–1120.

[CSI, 2012] CSI (2012). SAP 2000 Integrated Software for Structural Analysis and Design - Version 15.

[Deierlein et al., 2003] Deierlein, G. G., Krawinkler, H., and Cornell, C. A. (2003). A framework for performance-based earthquake engineering. *2003 Pacific Conference on Earthquake Engineering*, 273(140):140–148.

[Dunbar et al., 2013] Dunbar, A., Pampanin, S., Palermo, A., and Buchanan, A. (2013). Seismic Design of Core-walls for Multi-Storey Timber Buildings. In *New Zealand Society of Earthquake Engineering Conference*.

[DYWIDAG-Systems International, 2015] DYWIDAG-Systems International (2015). DYWIDAG Post-Tensioning System using Bars.

[Eatherton et al., 2008] Eatherton, M., Hajjar, J., Deirerlein, G., Krawinkler, H., Billington, S., and Ma, X. (2008). Controlled rocking of steel-framed buildings with replaceable energy-dissipating fuses. *14th World Conference on Earthquake Engineering*.

[Element5, 2019] Element5 (2019). Element5 Co.

[European Committee for Standardization, 2004] European Committee for Standardization (2004). *Eurocode 5: Design of timber structures. Part 1-1: General - Common rules and rules for buildins.* EN 1995-1-1, Brussels.

[FEMA, 1997] FEMA (1997). NEHRP Guidelines for the Seismic Rehabilitation of Buildings: FEMA 273. Technical report.

[FEMA, 2003] FEMA (2003). NEHRP Recommended Provisions for Seismic Regulations of New Buildings and Other Structures: FEMA 450. Technical report, Federal Emergancy Management Agency, Washington, D.C.

[Fib, 2003] Fib (2003). Displacement-based seismic design of reinforced concrete buildings. Technical report, International Federation for Structural Concrete, Lausanne, Switzerland.

[Gagnon and Pirvu, 2011] Gagnon, S. and Pirvu, C., editors (2011). *CLT Handbook: Cross-laminated timber*. FPInnovations, Quebec City, canadian edition.

[Ganey, 2015] Ganey, R. (2015). Seismic Design and Testing of Rocking Cross Laminated Timber Walls. University of Washington.

[Iqbal et al., 2007] Iqbal, A., Pampanin, S., Buchanan, A., Fragiacomo, M., and Palermo, A. (2007). Application of Hysteretic Dampers in LVL Coupled Walls for Improved Seismic Performance. In *Proceedings, 8th Pacific Conference of Earthquake Engineering*, Singapore.

[Kovacs and Wiebe, 2017] Kovacs, M. and Wiebe, L. (2017). Controlled Rocking CLT Walls for Buildings in Regions of Moderate Seismicity: Design Procedure and Numerical Collapse Assessment. *Journal of Earthquake Engineering*, 23(6).

[Krawinkler, 1999] Krawinkler, H. (1999). Challenges and progress in performance-based earthquake engineering. *International Seminar on Seismic Engineering for Tomorrow*, pages 1–10.

[Krawinkler and Miranda, 2004] Krawinkler, H. and Miranda, E. (2004). Performance-Based Earthquake Engineering. In Bozorgnia, Y. and Bertero, V. V., editors, *Earthquake Engineering: From Engineering Seismology to Performance-Based Engineering*, pages 1–85 of chapter 4. CRC Press.

[Kreuzinger, 1995] Kreuzinger, H. (1995). Mechanically jointed beams and columns. In *Timber Engineering - STEP 1*. B11/1-8, Almere.

[Kurama et al., 1999] Kurama, Y., Sause, R., Pessiki, S., and Lu, L.-W. (1999). Lateral load behavior and seismic design of unbonded post-tensioned precast concrete walls. *ACI Structural Journal*, 96(4).

[Kurama and Shen, 2004] Kurama, Y. and Shen, Q. (2004). Posttensioned hybrid coupled walls under lateral loads. *Journal of structural Engineering*, 130(2):297–309.

[Laursen and Ingham, 2001] Laursen, P. and Ingham, J. (2001). Structural Testing of Single-Storey Post-Tensioned Concrete Masonry Walls. *Journal of The Masonry Society*, 19(1):69–82.

[Laursen and Ingham, 2004] Laursen, P. and Ingham, J. (2004). Structural testing of large-scale posttensioned concrete masonry walls. *ASCE Journal of Structural Engineering*, 130(10):1497–1505.

[Marriott, 2009] Marriott, D. (2009). The Development of High-Performance Post-Tensioned Rocking Systems for the Seismic Design of Structures. Universtiy of Canterbury.

[Morris et al., 2012] Morris, H., Wang, M., and Zhu, X. (2012). *Deformations and Loads in an LVL Building with 3-Storey Post-Tensioned Shear Walls*. Auckland, New Zealand.

[Nakaki, S.D., Stanton, J.F., Sritharan, 1999] Nakaki, S.D., Stanton, J.F., Sritharan, S. (1999). An overview of the PRESSS five-story precast test building. *PCI journal*, 44(2):26–26.

[Newcombe, 2005] Newcombe, M. (2005). *Seismic Resisting Structural Systems using Laminated Veneer Lumber*. 3rd professional project, University of Canterbury, Christchurch.

[Newcombe, 2008] Newcombe, M. (2008). *Seismic Design of Multistorey Post-Tensioned Timber Buildings*. Masters thesis, University of Pavia, Pavia, Italy.

[Newcombe, 2011] Newcombe, M. P. (2011). *Seismic Design of Post-Tensioned Timber Frame and Wall Buildings*. PhD thesis, University of Canterbury.

[Newcombe, 2015] Newcombe, M. P. (2015). The Connection Response of Rocking Timber Walls. *SESOC Journal*, 28(1):46–53.

[Newcombe et al., 2008] Newcombe, M. P., Pampanin, S., Buchanan, A., and Palermo, A. (2008). Section Analysis and Cyclic Behavior of Post-Tensioned Jointed Ductile Connections for Multi-Story Timber Buildings. *Journal of Earthquake Engineering*, 12(S1):83–110.

[NRCC, 2015] NRCC (2015). *National Building Code of Canada*. Canadian Commission on Building and Fire Codes.

[Palermo and Pampanin, 2008] Palermo, A. and Pampanin, S. (2008). Analysis and simplified design of precast jointed ductile connections. In *World Conference on Earthquake Engineering*, Beijing, China.

[Palermo et al., 2006] Palermo, A., Pampanin, S., and Buchanan, A. (2006). Experimental investigations on LVL seismic resistant wall and frame subassemblies. In *First European Conference in Seismic Engineering and Seismology (a joint event of the 13th ECEE & 30th General Assembly of the ESC)*, Geneva, Switzerland.

[Palermo et al., 2005] Palermo, a., Pampanin, S., Buchanan, A., and Newcombe, M. (2005). Seismic design of multi-storey buildings using laminated veneer lumber (LVL). *NZSEE Conference*.

[Pampanin et al., 2002] Pampanin, S., Christopoulos, C., and Priestley, M. J. N. (2002). *Residual Deformations in the Performance-Based Seismic Assessment of Frame Structures*. IUSS Press, Pavia, Italy.

[Pampanin et al., 2001] Pampanin, S., Priestley, M. J. N., and Sritharan, S. (2001). Analytical Modelling of the Seismic Behaviour of Precast Concrete Frames Designed With Ductile Connections. *Journal of Earthquake Engineering*, 5(3):329–367.

[Parker and Steenkamp, 2012] Parker, M. and Steenkamp, D. (2012). The economic impact of the Canterbury earthquakes. *Reserve Bank of New Zealand: Bulletin*, 75(3):13–25.

[Priestley, 1991] Priestley, M. J. N. (1991). Overview of the PRESSS Research Programme. *PCI Journal*, 36(4):50–57.

[Priestley, 2000] Priestley, M. J. N. (2000). Performance based seismic design. *12th WCEE*, 1(1):1–22.

[Priestley et al., 1999] Priestley, M. J. N., Sritharan, S., Conley, J. R., and Pampanin, S. (1999). Preliminary Results and Conclusions from the PRESSS Five-story Precast Concrete Test- Building. *PCI Journal*, 44(6):42–67.

[Reinoso and Miranda, 2005] Reinoso, E. and Miranda, E. (2005). Estimation of floor acceleration demands in high-rise buildings during earthquakes. *The Structural Design of Tall and Special Buildings*, 14(2):107–130.

[Ricles et al., 2001] Ricles, J. M., Sause, R., and Garlock, M. M. (2001). Experimental studies of full-scale post-tensioned steel connections. *Journal of Structural Engineering*, 131(3):113–121.

[Rosenboom and Kowalsky, 2004] Rosenboom, O. A. and Kowalsky, M. J. (2004). Reversed in-plane cyclic behavior of post-tensioned clay brick masonry walls. *Journal of Structural Engineering*, 130(5):787–798.

[Sarti, 2015] Sarti, F. (2015). *Seismic Design of Low - Damage Post - Tensioned Timber Wall Systems*. PhD thesis, University of Canterbury.

[SEAOC, 1995] SEAOC (1995). *VISION 2000 - Performance Based Seismic Engineering of Buildings*, volume I. Sacramento, California.

[Smith et al., 2007] Smith, T., Ludwig, F., Pampanin, S., Fragiacomo, M., Buchanan, A., and Deam, B. (2007). *Seismic response of Hybrid-LVL coupled walls under quasi-static and pseudo-dynamic testing*. NZSEE Conference, Palmerston North, New Zealand.

[Smith et al., 2008] Smith, T., Pampanin, S., Buchanan, A., and Fragiacomo, M. (2008). Feasibility and de- tailing of post-tensioned timber buildings for seismic areas. In *NZSEE Conference*.

[Structural Timber Innovation Company, 2013] Structural Timber Innovation Company (2013). Design Guide Australia and New Zealand- Post-Tensioned Timber Buildings. *Structural Timber Innovation Company. Christchurch, New Zealand*.

[Wiebe, 2013] Wiebe, L. (2013). *Design of Controlled Rocking Steel Frames to Limit Higher Mode Effects*. PhD thesis, University of Toronto.

[Yeoh et al., 2012] Yeoh, D., Carradine, D., Palermo, A., Shrestha, R., and Morris, H. (2012). *Long-Term Performance of Post-Tensioned LVL Frames and Walls.* Canterbury, NZ.

[Zhang et al., 2018] Zhang, C., Steele, T. C., and Wiebe, L. (2018). Design-level estimation of seismic displacements for self-centering SDOF systems on stiff soil. *Engineering Structures*, 117:431–443.

Appendix A - Material Tests

Material properties for the CLT panels were obtained through compression tests in the primary orientation of both 3-ply and 5-ply test specimens, shown in Figure A.1. The specimen panels obtained from the manufacturer were cut into columns. Ten 5-ply, and six 3-ply tests were performed. In addition to the varying thickness, the width and height of the specimens varied. The thickness and width were multiplied to calculate the area of each specimen. The Shimadzu universal hydraulic test frame (UH-FX) used for the specimen tests provided reading of force and head displacement, with a capacity of 1000 kN. Stress was determined by dividing the measured force by the specimen area, while the strain was obtained by dividing the head displacement by the total height of the specimen.

(a) 3-Ply and 5-Ply Material Test Specimens

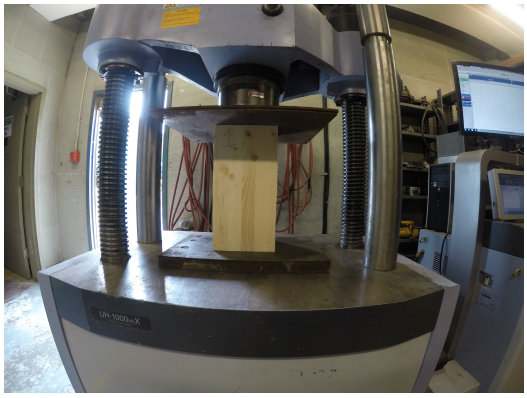

(b) Specimen 1 in Universal Hydraulic Test Frame

Figure A.1: CLT Panel Material Tests

In order to obtain the modulus of elasticity, E, a linear regression of the elastic region of the stress versus strain plot for each test, between 1MPa and 18MPa, was performed. The modulus of elasticity was taken as the slope of the linear regression. The modulus of elasticity of both the 3-ply and 5-ply used for analysis in this thesis is the average of all the test specimens. Similarly, the yield strength in compression, f_y, is taken as the compressive strength, as per [Kovacs and Wiebe, 2017], and is the maximum stress the specimen achieved. The average compressive strength was used for analysis in this thesis. The stress versus strain data is shown in Figures A.2 and A.3. The test specimen data is shown in Table A.1. Test 3.6 was identified as an outlier and not included in the

average. Also provided is the manufacturer's pre-fabrication estimate of the material properties.

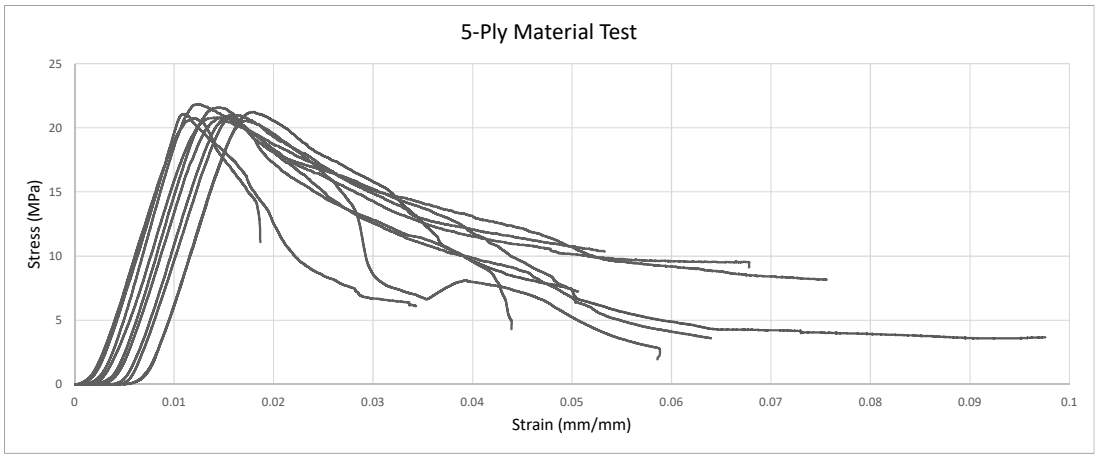

Figure A.2: 5-Ply Stress vs. Strain Material Test Curve

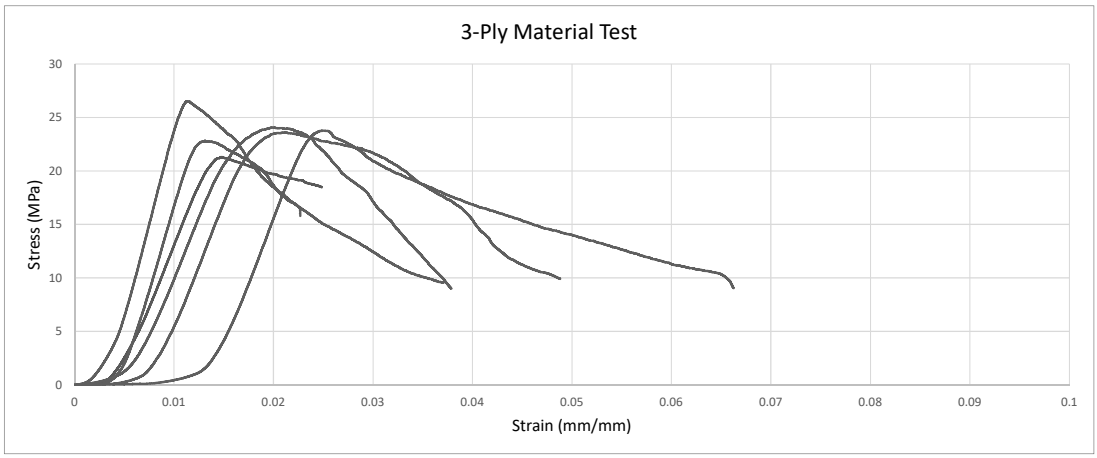

Figure A.3: 3-Ply Stress vs. Strain Material Test Curve

Table A.1: Material Test Results

Test	*Area* (mm^2)	*Height* *(mm)*	*E* *(MPa)*	f_y *(MPa)*
5.1	32000	410	2236	21.23
5.2	32000	410	2408	20.73
5.3	32000	410	2412	20.55
5.4	32000	410	2382	20.85
5.5	32000	410	2275	20.82
5.6	32000	410	2372	20.99
5.7	32000	410	2287	20.8
5.8	32000	410	2572	21.07
5.9	41600	510	2569	21.59
5.10	38400	510	2577	21.85
	Mean		2409	21.048
	Stand. Dev.		121	0.38
3.1	39360	410	2313	21.30
3.2	39360	410	2238	23.78
3.3	39360	410	2182	23.60
3.4	39360	410	2157	24.07
3.5	24000	510	2845	22.81
3.6	24000	510	3622	26.54
	Mean		2347	23.11
	Stand. Dev.		255	0.99
Manufacturer Pre-Fab. Est.			6435	N/A